Geomech. Geophys. Geo-energ. Geo-resour. (2026) 12:49
https://doi.org/10.1007/s40948-026-01119-5

RESEARCH

Development of continuous estimates of the least principal stress with depth for application to multi-stage hydraulic fracturing

Mark D. Zoback · Ankush Singh

Received: 19 October 2025 / Accepted: 26 January 2026

Abstract Obtaining accurate knowledge of variations in the magnitude of the least horizontal principal stress, S_{hmin}, with depth is of great practical importance in the oil and gas industry. We demonstrate that accurate knowledge of the magnitude of S_{hmin} with depth can be obtained utilizing two fundamental concepts. First, frictional faulting constraints place bounds on principal stress magnitudes in relatively stiff (high Young's modulus) rocks. These bounds depend on depth, pore pressure and whether a site is characterized by a normal, strike-slip or reverse faulting stress state. Second, in more ductile clay-rich formations such as those typical of most US unconventional plays, varying degrees of viscoplastic stress relaxation (VSR) reduces differences between principal stress magnitudes. We focus in this paper on the importance of how layer-to-layer variations of lithology control the magnitude of S_{hmin} and how the two concepts above can be used to accurately predict variations of the magnitude of S_{hmin} with depth. It is well established that the effectiveness of multistage hydraulic fracturing is critical to stimulate production in unconventional oil and gas reservoirs. Using several case studies, we illustrate how predictable variations of stress magnitude with depth affect hydraulic fracture propagation. We also demonstrate that widely used elastic loading models do not accurately predict variations with depth. In the context of VSR, essentially complete stress relaxation also helps explain occasional observations of the least principal stress being nearly equal to the overburden stress in some clay-rich formations. In such cases, sub-horizontal hydraulic fracture propagation is expected due to the low tensile strength of bedding planes.

Highlights

- We review several case studies that document lithology-dependent variations of S_{hmin} magnitude with depth. These layer-to-layer stress variations, sometimes as large as 10 MPa (~1500 psi), have a profound effect on hydraulic fracture propagation.
- To create continuous estimates of the magnitude of S_{hmin} with depth, we present a methodology that combines the concept of frictional failure equilibrium in relatively stiff formations with that of viscoplastic stress relaxation in more ductile formations.
- We demonstrate how quantitative estimates of S_{hmin} magnitude with depth obtained using the concept of viscoplastic stress relaxation significantly improves prediction of hydraulic fracture propagation.

M. D. Zoback (✉)
Stanford University, Stanford, CA 94305, USA
e-mail: zoback@stanford.edu

M. D. Zoback · A. Singh
ResFrac Corporation, Palo Alto, CA 94301, USA
e-mail: ankush@resfrac.com

Published online: 25 February 2026

- We demonstrate that this approach yields more accurate estimates of S_{hmin} magnitude than commonly used elastic loading stress prediction methods.
- We illustrate cases of near-complete stress relaxation (meaning that the three principal stresses become co-equal). In the absence of stress control, hydraulic fracture propagation occurs along weak, sub-horizontal bedding planes.

Keywords Stress magnitude prediction with depth · Hydraulic fracture propagation · Viscoelastic stress relaxation · Horizontal hydraulic fracture propagation

1 Introduction

It is well-established that hydraulic fracture propagation is controlled by the magnitude and orientation of the least principal stress (Hubbert and Willis, 1957). In nearly all cases of relevance for unconventional oil and gas development, the least principal stress is the minimum horizontal principal stress, S_{hmin}, such that hydraulic fractures propagate in a near vertical plane-oriented perpendicular to S_{hmin}. While a great deal of observational evidence has supported this fundamental concept over the past 68 years, it has recently been validated by hydraulic fracture drill-through experiments (Raterman et al. 2017; Gale et al., 2018), fiber optic studies in offset horizontal wells (Barhaug et al. 2022; Ugueto et al. 2022) and hydraulic fracture trends implied by microearthquake alignments which are in agreement with independent data on in situ stress orientation (Lund Snee and Zoback 2022).

Equally important to knowing the direction of hydraulic fracture propagation is knowing how variations of S_{hmin} magnitude affect horizontal hydraulic fracture propagation. For example, Dohmen et al. (2017) used microseismic data to demonstrate how asymmetric lateral hydraulic fracture propagation occurs from a newly-drilled *child* well in the Bakken formation near a depleted *parent* well (Cipolla et al. 2022). The microseismic data clearly show how the hydraulic fractures preferentially propagate away from a child well toward the depleted zone surrounding a nearby parent well. This occurs because of the poroelastic decrease in stress magnitudes associated with depletion. Thus, opening Mode 1 hydraulic fractures propagate perpendicular to the least principal stress in a minimum energy configuration.

In practice, in order to assess the relative degree of horizontal versus vertical hydraulic fracture propagation, variations of stress magnitude with depth are also of first order importance. It affects optimal choices of landing depths and well spacings (e.g., Singh et al. 2019, Fowler et al. 2024). The simplest case of stress magnitude variations with depth is a monotonic variation of the magnitude of S_{hmin} as hydraulic fractures will propagate upward, or downward, depending on whether S_{hmin} increases or decreases with depth. As a given hydraulic fracturing stage has a specific volume of fracturing fluid and proppant, excessive vertical propagation of a hydraulic fracture obviously results in less horizontal propagation (e.g., Zoback et al. 2022). This could have two negative consequences: First, there could be unwanted stimulation of non-hydrocarbon bearing (perhaps water bearing) formations above or below the pay zone. Second, at the depth of the pay zone, much closer spacings between horizontal wells will be required to optimize production. In the case of exploiting *stacked pay* (places where there are multiple hydrocarbon-bearing formations at different depths), optimal well spacing could vary markedly for pay zones at different depths when there is appreciable vertical propagation at some depths (e.g., McClure et al. 2023). In this paper we address practical methodologies for determining S_{hmin} magnitude variations with depth and the importance of understanding stress variations with depth for optimizing hydraulic fracture stimulation. While many factors affect successful multi-stage hydraulic fracturing operations, as illustrated below, optimizing hydrocarbon recovery from unconventional wells requires understanding how stress variations with depth affect the interplay between vertical and horizontal hydraulic fracture propagation.

In Sect. 2 we present three case studies where numerous direct measurements of S_{hmin} (via mini-frac or DFIT tests) document lithologically-controlled layer-to-layer variations of the magnitude of S_{hmin} with depth. These variations are sometimes as large as 1500 psi (~10 MPa). Section 3 briefly reviews three approaches that can be used to estimate the magnitude of S_{hmin} with depth: First, we review limits on differential stress magnitudes imposed by the frictional strength of pre-existing faults distributed throughout the crust. These limits depend on depth,

pore pressure and whether a site is characterized by a normal, strike-slip or reverse faulting stress state. Knowledge of variations of all three principal stresses with depth are of importance to address problems wellbore stability and fault re-activation (e.g., Zoback 2007). We next review stress magnitudes predicted by the assuming instantaneous loading in an elastic, layered earth (Eaton 1969; Blanton and Olson 1999; Thiercelin and Plumb 1994). As we point out, while there are a number of assumptions associated with elastic loading models that are highly questionable, these methods have been widely used for decades because they offer the possibility to predict continuous profiles of stress magnitude with depth. Finally in Sect. 3, we combine the concepts of frictional equilibrium in relatively brittle rocks with the concept of viscoplastic reduction of differential stress magnitudes in relatively ductile formations. This approach also makes it possible to estimate continuous profiles of S_{hmin} with depth (e.g., Sone and Zoback 2014a; Singh and Zoback 2022).

In Sect. 4 we show how stress magnitude predictions incorporating the concept of VSR can be used effectively, whether in a qualitative, approximate or detailed manner. The VSR concept allows us to explain cases in which direct measurements of $S_{\mathrm{hmin}} \approx S_V$ (complete stress relaxation) in clay-rich rocks, regardless of whether it is a normal or strike-slip stress state. An interesting aspect of complete stress relaxation is that in absence of hydraulic fracture propagation being controlled by the stress field as the three principal stresses are expected to be co-equal, hydraulic fractures will most likely to propagate along weak, sub-horizontal bedding planes (Dontsov et al. 2026). Section 5 presents comparisons of stress magnitude predictions with depth between the elastic loading and viscoplastic stress relaxation models and its importance on accurate prediction of hydraulic fracture propagation.

2 Direct measurements of S_{hmin} magnitude variations with depth

In this section, we review several case studies where numerous direct measurements of the magnitude of $S_{h\mathrm{min}}$ show considerable variability with depth that correlates with lithology. It is obvious in the next four figures (and well established over decades of study) that $S_{h\mathrm{min}}$ in oil and gas wells can be accurately determined by some form of hydraulic fracturing. The tests might be called mini-fracs or micro-fracs because a very small amount of fluid is pumped into the hydraulic fracture or an extended leak-off test (in which a hydraulic fracture is induced in a limited open-hole section at the end of a cased and cemented well or a DFIT (Dynamic Fracture Injection Test) which begins with a mini-frac and thus provides a direct measure of $S_{h\mathrm{min}}$. Pore pressure and permeability can also be determined from DFIT tests (McClure et al. 2022). Figure 1 shows $S_{h\mathrm{min}}$ measurements from a group of wells at the HFTS 1 test site in the Midland Basin of west Texas (modified from Kohli and Zoback 2021). Lund Snee and Zoback (2022) show that this area is characterized by a normal/strike-slip faulting stress state ($S_V \approx S_{H\mathrm{max}} \geq S_{h\mathrm{min}}$). Figure 1a shows the geometry of the horizontal wells at the site in a stratigraphic coordinate system. In other words, the well positions were slightly adjusted so that each well is shown with respect to the stratigraphic boundaries above and below, using for reference the vertical 7SU pilot well which was thoroughly logged. Figure 1b shows the clay + TOC (total organic content) from geochemical logs in the pilot well. Measurements of the least principal stresses come from DFIT tests in the pilot well and the toes of the horizontal wells. Additional $S_{h\mathrm{min}}$ values are indicated from individual frac stages in the horizontal wells when distinct Instantaneous Shut-in Pressures (ISIPs) could be seen. Note that the layer-to-layer differences of the measured $S_{h\mathrm{min}}$ values (which vary by as much as ~ 10 MPa, ~ 1500 psi) are correlative with the relative amounts of clay plus organic content in the formation. The two shaded areas in Figs. 1b, c are at the depths of the horizontal wells which are concentrated in the lower part of unit Upper Wolfcamp 2 (UW2) and lower part of Middle Wolfcamp 1 (MW1) lithofacies. Not surprisingly, both depth intervals are intervals where there is high clay + TOC. Note that both intervals are also characterized by high values of $S_{h\mathrm{min}}$. It is noteworthy that the four DFIT tests that show very low values of $S_{h\mathrm{min}}$ are in lithofacies with very low clay + TOC. Moreover, at the upper and lower boundaries of the UW2 and MW1 lithofacies, the magnitude of $S_{h\mathrm{min}}$ changes significantly over small depth intervals as there are abrupt changes in lithology. This is clearly seen at the upper and lower boundaries of the shaded intervals where the wells are concentrated. The blocked line

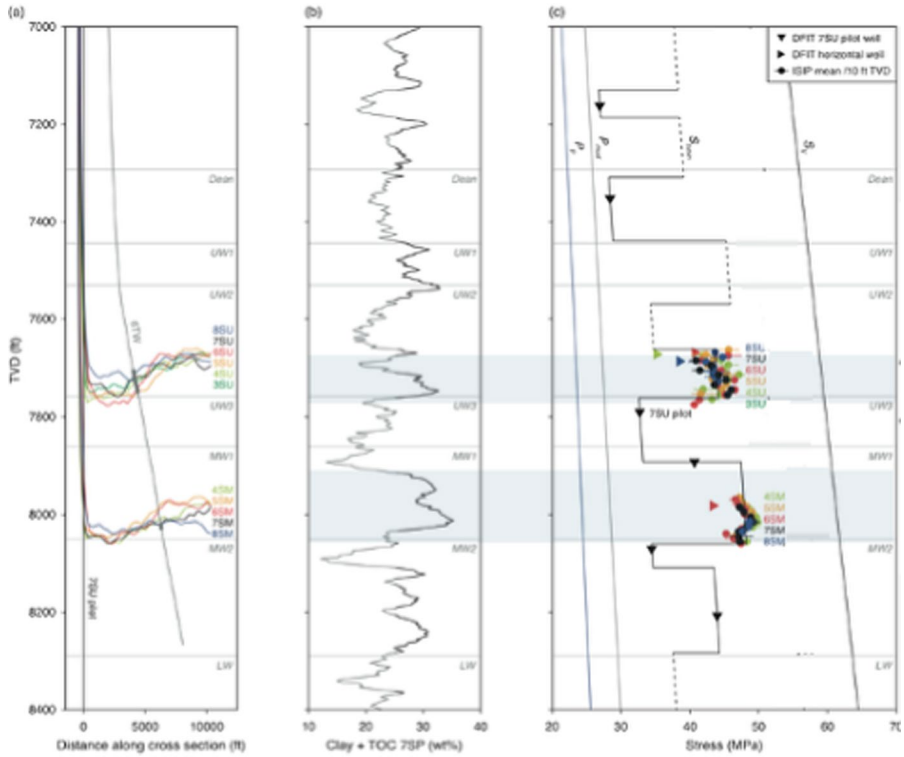

Fig. 1 The relationship between variations of clay plus organic content of the relevant lithologic units at the HFTS-1 test side in the Midland basin (adapted from Kohli and Zoback 2021). TVD represents true vertical depth, in feet. **a** The trajectories of relevant wells at the HFTS-1 test site relative to formation boundaries in the 7SU pilot well. **b** The relative weight percent of clay + TOC as determined from geochemical logs in the 7SU pilot well. **c** The magnitude of the least principal stress at various depths from DFIT measurements and distinct shut-in pressures from some of the frac stages. The Mohr circle at ~ 7800 ft. is in lithologic units with relatively small amounts of clay plus kerogen. As explained in the text, the relatively low values of S_{hmin} in these lithologic units are explained well by frictional faulting theory for a normal faulting environment, as shown by the Mohr circle and explained in the text. The Mohr circles at about 7700 ft are for a lithologic unit with relatively high clay plus TOC. The names of the formations associated with the abbreviations shown are as follows: UW1 (Upper Wolfcamp 1), UW2 (Upper Wolfcamp 2), UW3 (Upper Wolfcamp 3), MW1 (Middle Wolfcamp 1), MW2 (Middle Wolfcamp 2), LW (Lower Wolfcamp)

in Fig. 1c indicates layer-to-layer variations of $S_{h\mathrm{min}}$ based on available measurements (solid line) and inferred values (dotted line) based on the clay + TOC content. The correlation between stress magnitude and clay + TOC intervals is clear.

Figure 2 shows a horizontal well drilled in the Woodford formation in Oklahoma (from Ma and Zoback 2017). Lund Snee and Zoback (2022) show that this is an area characterized by strike-slip faulting ($S_{H\mathrm{max}} \geq S_V \geq S_{h\mathrm{min}}$). The upper part of the figure shows the clay + TOC content as measured with an elemental spectroscopy logging tool (the fluctuating gray line with the black line representing the median), the values of the least principal stress as determined from ISIPs of individual stages (red dots with sticks) and the amount of proppant injected during each stage (blue bars). The lower panel shows the well path, position of the stages, the median clay plus TOC content as well as three distinct lithofacies of the Woodford (WDFD-1, WDFD-2 and WDFD-3) that were defined on the basis of compositional data obtained from a nearby vertical well. What appears to be severe undulation of the well path is an artifact of the extreme exaggeration of the vertical scale. The toe of each of these ~ 4000 ft lateral wells is only 10's of ft above the heel. In both wells, note that whenever the well trace deviates out of the WDFD-2 lithofacies, there is a marked increase in the magnitude of the

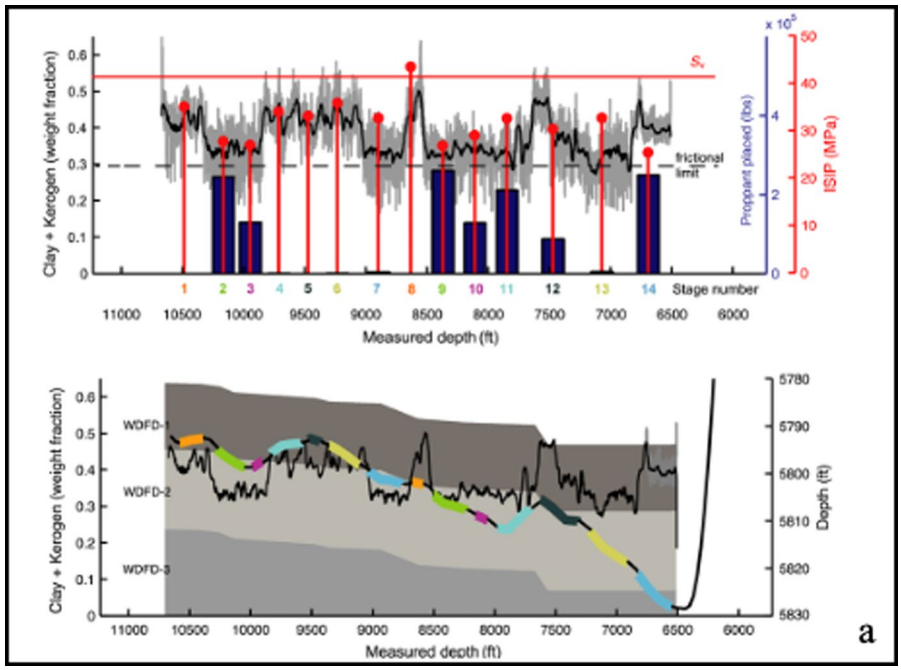

Fig. 2 Stage by stage S_{hmin} measurements in a horizontal well in the Woodford formation, Oklahoma shows a strong correlation between clay plus kerogen content and stress magnitude (From Ma and Zoback 2017). Each figure shows the variation of clay plus kerogen content (black curve represents the smoothed log readings in gray). The ISIP values (shown by red dots) and the amount of proppant placed during each HF stage (blue bars). The ISIP and place proppant amount are positioned at the middle of the respective stages. The horizontal red line indicates the magnitude of overburden stress. The dashed black line indicates the magnitude of S_{hmin} at which normal faulting would occur as explained below. The lower panel shows the well trajectory (note the exaggerated vertical scale) and the content of clay plus kerogen along the well and separation of the Woodford into the WDFD-1, 2 and 3 lithofacies

least principal stress. Thus, what appears to be variability of the magnitude of $S_{h\mathrm{min}}$ along the length of the lateral is actually a variation of stress with depth as sampled by the undulating well path. Ma and Zoback (2017) showed that the high magnitudes of $S_{h\mathrm{min}}$ in the WDFD-1 lithofacies was confirmed by DFIT tests in the toe of each of the two wells. Note that the ISIP's indicate that the magnitude of $S_{h\mathrm{min}}$ along the length of the well varies by over 10 MPa. Note also the excellent correlation between the magnitude of the least principal stress gradient with clay + TOC content. For the case of stage 8 of the well shown in Fig. 2a, the least principal stress is approximately equal to the vertical stress and that the clay plus kerogen content was quite high. The same was seen for stages 2 and 7 in another well and there is an excellent correlation between the clay and kerogen content and the frac gradient i as well. In both cases, the stages with the highest frac gradient are those with the highest clay plus kerogen content. Theoretically, the magnitude of the least principal stress can never exceed the vertical stress. Thus, the observations that the measured value of the least principal stress slightly exceeds the vertical stress in a couple of cases probably reflects uncertainty in estimating $S_{h\mathrm{min}}$ from the shut-in pressures of individual frac stages instead of mini-frac or DFIT tests. Nonetheless, the consistency of multiple measurements and multiple types of measurements seen in Fig. 1 gives us confidence that the shut-in pressures from frac stages, when distinct, yield reliable estimates of the magnitude of $S_{h\mathrm{min}}$.

Another example of observed differences in the magnitude of measured values of $S_{h\mathrm{min}}$ with depth that correlate with lithology is the large number of minifrac measurements made in three vertical wells drilled in close proximity near the town of Rulison, Colorado, an area characterized by normal faulting ($S_V \geq S_{H\mathrm{max}} \geq S_{h\mathrm{min}}$). These stress measurements were carried out in the 1980's in the Multiwell Experiment (reported by Warpinski et al. 1985). A compilation of

the S_{hmin} measurements is shown in Fig. 3 (modified from Nelson, 2003) along with pore pressure measurements and inferences about pore pressure from mud weights during drilling. The measured values of S_{hmin} in sands (inverted yellow triangles) increase with depth as predicted by frictional faulting theory (which is discussed below), taking into account the increase in pore pressure with depth (blue triangles). In marked contrast, the stress measurements in the clay-rich shales and mudstones are much higher than the values in the sands and almost all are very close to the magnitude of the vertical stress, indicating an essentially isotropic stress state. We argue below that the values of the minimum principal stress being essentially equal to the vertical stress is due to essentially complete viscoplastic stress relaxation in clay rich rocks.

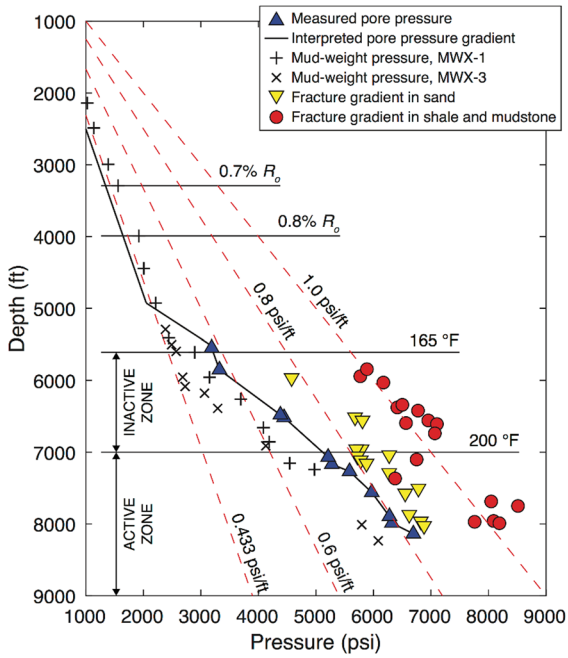

Fig. 3 Least principal stress and pore pressure measurements in a layered sequence of sands and shales from three closely-spaced wells that were part of the Multiwell Experiment (MWX) in western Colorado. Elevated pore pressure (blue triangles) was observed at depth in three wells. The least principal stress, S_{hmin}, in sands (inverted yellow triangles) increases as the pore pressure, Pp, increases whereas stress measurements in shales (red dots) are mostly close to the vertical stress, S_V (~ 1 psi/ft), indicating near complete stress relaxation. Adapted from Nelson (2003)

Figure 4 (from Alalli and Zoback 2018) shows a case study from the Marcellus play in West Virginia, an area Lund Snee and Zoback (2022) show is characterized by strike-slip/reverse faulting ($S_{H\max} \geq S_V \approx S_{h\min}$). The microseismic event distribution for stages 11–17 show the microseismic events are essentially limited to the Lower Marcellus shale (LMRC) while the events associated with stages 18–21 (in the Cherry Valley Limestone, CVLR) show microseismic events extend upward over 500 ft. There was no microseismic recording during stages 1–10. The lower panel of Fig. 4 shows the measured shut-in pressures (red dots). Note that for stages 1–16 in the LMRC, the ISIPs were approximately equal to (or slightly greater than) S_V, while stages 17–20 in the CVLS show the measured ISIPs to be less than S_V, thus corresponding to $S_{h\min}$. Both the values of the least principal stress for stages 1–16 as well as the distribution of microseismic events for stages 11–16 appear to indicate sub-horizontal hydraulic fracture propagation.

3 Methods to estimate S_{hmin} as a function of depth

In this section we briefly review three approaches to estimate a continuous profile of the magnitude of $S_{h\min}$ with depth that can be practically implemented in the oil and gas industry. One of the most important reasons for determining the magnitude of $S_{h\min}$ at depth is to select optimal mud weights during drilling. Safe drilling operations require mud weights to be greater than pore pressure to avoid kicks (hydrocarbons coming into the well) but less than the least principal stress to avoid unintentionally inducing hydraulic fractures during drilling. In fact, estimating this "safe mud weight window" was one of the primary motivations for stress estimation method proposed by Eaton (1969) that is discussed below.

3.1 Frictional constraints on stress magnitudes

The idea that the frictional strength of pre-existing faults in the crust put limits on stress magnitudes was first proposed conceptually by (Sibson 1974) and later expanded upon by Zoback and Healy (1984) in the context of available stress measurements at that time. The basis for these limiting stress magnitudes is that over the scale of reasonable crustal volumes, faults are present with a wide range of orientations

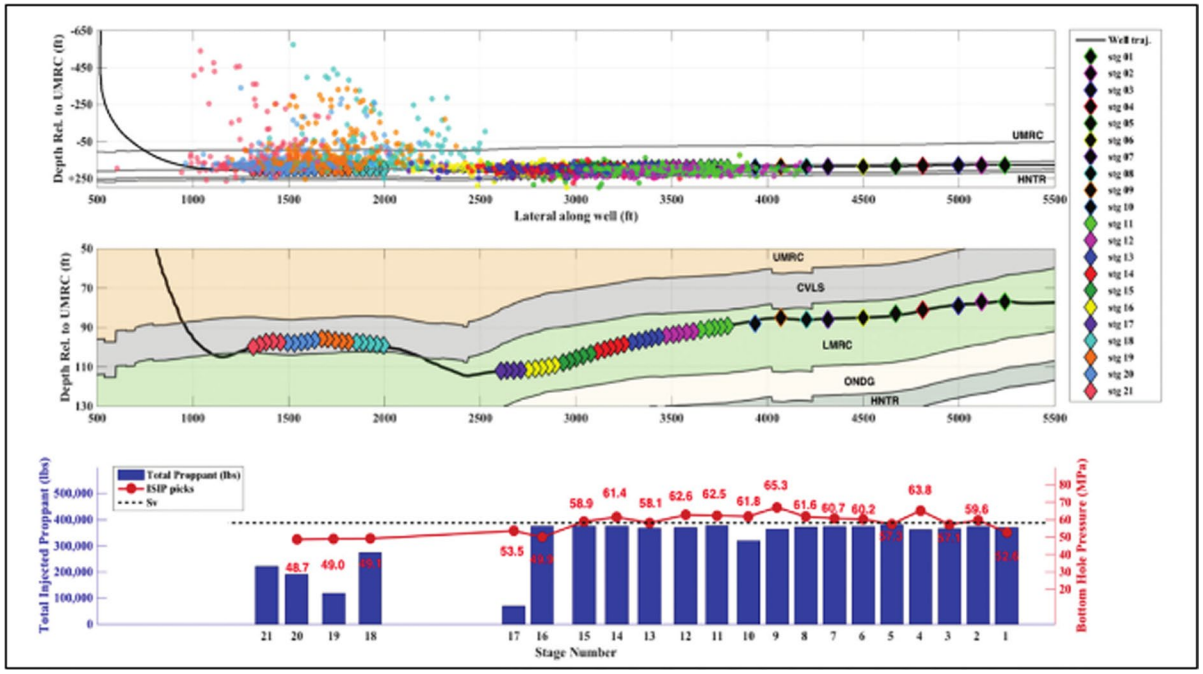

Fig. 4 A profile view of microseismic event distribution along a well in the Marcellus formation for each fracturing stage; only stages 11–21 were monitored for microseismic activity. The middle panel is a vertically exaggerated section showing the well trajectory. The bottom panel plots total injected proppant volume (bar plot) and measured ISIP (red dots) relative to S_V (black dashed line) across all stages. From Alalli and Zoback (2018)

which are inherited over 100's of millions of years of geologic history. As episodes of geologic deformation cause stress magnitudes to change, frictional slip on the faults most well-oriented for failure can be predicted utilizing Coulomb faulting theory and laboratory-derived friction measurements (Byerlee 1978) regardless of when those faults first formed (as the stress required to overcome fault cohesion is negligible). While there is considerable support for this concept, most relevant are observations from a number of sedimentary basins around the world which shows this to also be true for relatively stiff sedimentary rocks (Zoback 2007).

It is helpful to briefly review key principles of Coulomb Faulting Theory that relate the current state of stress in relatively brittle rocks. Figures 5a-e represent commonly occurring stress states in regions of interest. The five stress states shown are an extension of Anderson faulting theory (Anderson 1951) as described by (Zoback and Kohli 2019). The five figures illustrate different configurations of the relative magnitudes of the vertical principal stress, S_V, the maximum horizontal principal stress, $S_{H\max}$, and the minimum horizontal principal stress, $S_{h\min}$ as well as the orientation of faults prone to reactivation for each stress state. In order of increasing compression, these stress states range continuously from.

- Normal faulting ($S_V \geq S_{H\max} \geq S_{h\min}$)-Fig. 5a
- Normal/strike-slip faulting ($S_V \approx S_{H\max} \geq S_{h\min}$)-Fig. 5b
- Strike-slip faulting ($S_{H\max} \geq S_V \geq$)-Fig. 5c
- Strike-slip/reverse ($S_{H\max} \approx S_V \geq S_{h\min}$)-Fig. 5d
- Reverse faulting ($S_{H\max} \geq S_{h\min} \geq S_V$)-Fig. 5e

To be able to map relative stress magnitude we quantify these stress states using the parameter A_ϕ (originally defined by Simpson 1997) which conveniently describes the ratio between principal stress magnitudes using a single, easily interpolated value. The background color in Fig. 5f (from Lund Snee and Zoback 2022) indicates A_ϕ values in central North America. As shown in Figs. 5a-e, an A_ϕ value of 0.5 indicates a normal faulting stress state, a value of 1.0 indicates a normal/strike-slip faulting stress state, and so on.

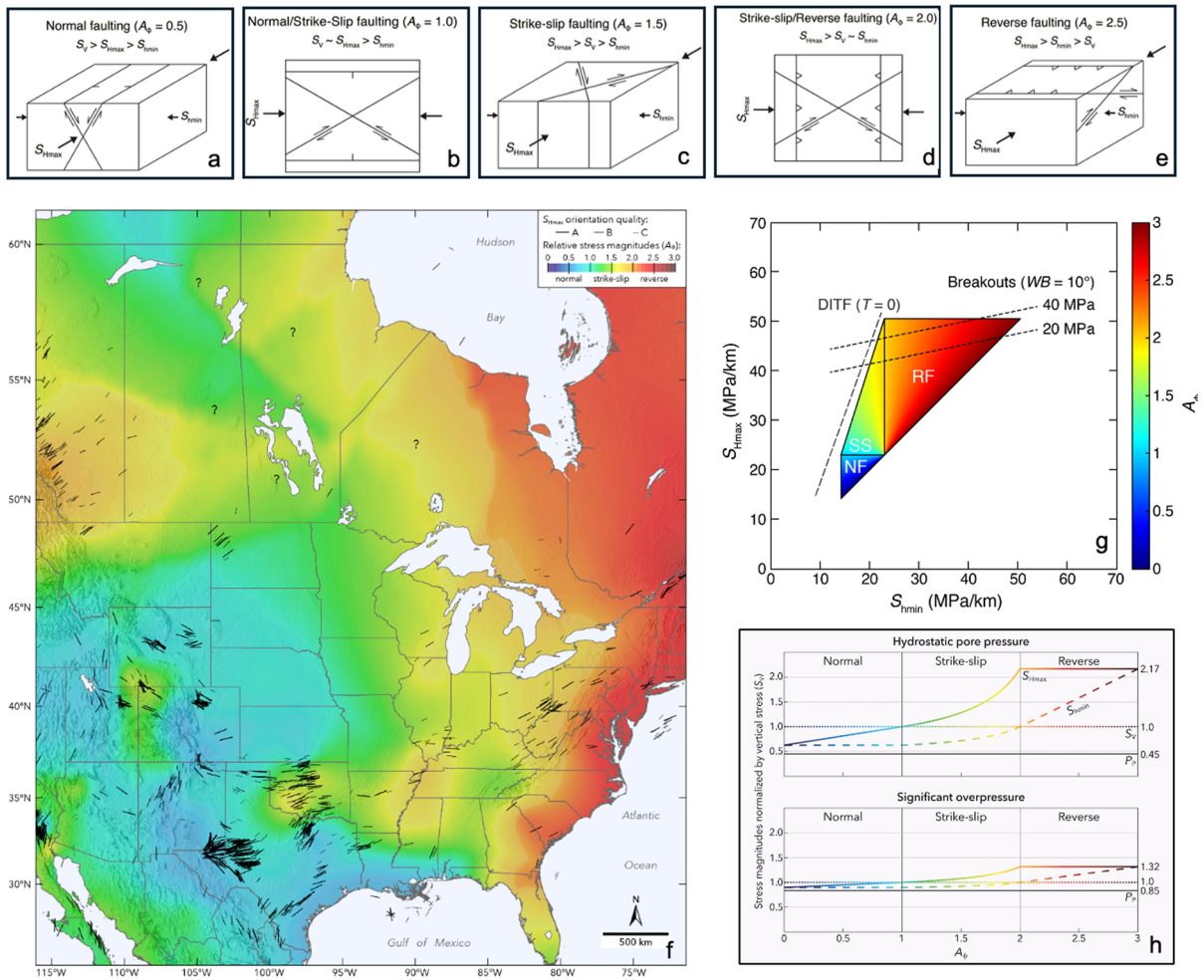

Fig. 5 **a-e** States of stress defined in the context of relative stress magnitudes **f** State of stress int he central and eastern U.S. The background color is a map of A_ϕ and the straight lines indicate the azimuth of S_{Hmax} in the regions of injection-induced seismicity discussed here. From Lund Snee and Zoback (2022). **g** A typical stress polygon that shows possible stress states at a given depth and pore pressure (see text). **h** Limiting values of stress magnitudes as a function of for hydrostatic pore pressure and elevate pore pressure equal to $0.85S_V$ (from Lund Snee and Zoback 2022)

The way to think about the faults shown in Figs. 5a-e, is that while faults of many orientations are likely to be present in an area, if the area is characterized by normal faulting (A_ϕ=0.5), as shown in Fig. 5a, a potentially active normal fault would be expected to strike parallel to the azimuth of S_{Hmax} and dip in the direction of S_{hmin} about 60° from horizontal (for expected values of the coefficient of friction of about 0.6). Similarly, as shown in Fig. 5c, potentially active strike-slip faults (A_ϕ=1.5) would be expected to dip steeply and strike ± 30° to the direction of S_{Hmax}. Reverse faults would be expected to dip about 30° and strike normal to the direction of S_{Hmax} as shown in Fig. 5e.

In terms of limiting stress magnitudes, slip on well-oriented faults will occur when the ratio of principal stresses satisfies the following equation (Jaeger et al. 2007).

$$(S_1 - P_p)/(S_3 - P_p) = (\sqrt{(\mu^2 + 1)} + \mu)^2 \quad (1)$$

where S_1 and S_3 refer to the maximum and minimum principal stresses in situ, Pp is pore pressure, μ is the coefficient of friction, taken to be 0.6 for sedimentary rocks with relatively low clay content. As noted above S_1

and S_3 depend on the stress state in a region. For normal faulting and normal/strike-slip faulting areas S_1 is the vertical stress, S_V and S_3 is least principal stress, $S_{h\min}$. In a normal faulting area, friction limits the lower bound of S_{hmin} (S_3) relative to S_V (S_1). In a strike-slip faulting stress state, friction limits the maximum difference between $S_{h\min}$ (S_3) and $S_{H\max}$ (S_1) and in a reverse faulting stress state, friction limits the upper bound of $S_{H\max}$ (S_1) with respect to S_V (S_3). The values of $S_{h\min}$ predicted by Eq. 1 fit the lower values of $S_{h\min}$ shown in Fig. 1 for relatively brittle rocks (see Kohli and Zoback 2021). In contrast, $S_{h\min}$ values are much higher in intervals with high clay plus TOC, such that the state of stress is not in frictional equilibrium (as indicated by the Mohr circle at approximately 7650 ft.).

The concept of stress magnitudes at any given depth being limited by the frictional strength of pre-existing faults gave rise to the stress polygon graphical representation (Fig. 5g, see Zoback 2007). Conceptually, the state of stress at a given depth and pore pressure have to within the limiting stress magnitudes indicated by the polygon. If the state of stress is consistent with the prediction of frictional faulting theory, the state of stress would fall along the periphery of the polygon. As noted above, this is found to be the case in relatively stiff sedimentary rocks in many areas. The most common usage of the stress polygon is when there is a measured value $S_{h\min}$, it is possible to constrain a maximum value of $S_{H\max}$ from the perspective of frictional limits on stress magnitude. However, the constraints based on frictional strength of pre-existing faults in the crust can be augmented by observations of the presence (or absence) of wellbore breakouts and/or drilling-induced tensile wall fractures. Thus, a few direct measurements of $S_{h\min}$ can be used to constrain the magnitude of $S_{H\max}$ which is needed to address problems related to wellbore stability and fault reactivation (see Zoback 2007).

Figure 5f is a stress map of the central North America. The straight lines indicate the direction of maximum horizontal compressive stress, $S_{H\max}$, which is obtained from wellbores in the sedimentary section and earthquake focal plane inversions in crystalline basement (see Lund Snee and Zoback 2022 for details). The length of each stress indicator is an indication of the quality of the measurement. The background color shows the relative stress magnitude via the parameter A_ϕ. Thus, with knowledge of both stress orientation and relative magnitude it is possible to infer limiting stress magnitudes as illustrated in Fig. 5h for hypothetical cases of near-hydrostatic and elevated pore pressure.

Figure 6 shows data (Zoback 2007) from five wells in the Travis Peak formation in east Texas, an area characterized by normal faulting. The $S_{h\min}$ from frictional faulting utilizing Eq. 1 are estimated for laboratory-determined values of $\mu = 0.6$ for all lithologies. The data clearly illustrates that for a range of lithologies in relatively stiff rocks frictional faulting theory accurately predicts $S_{h\min}$ over a range of depths and in different geologic settings. Other examples included the Nevada Test Site, South Eugene Island in the Gulf of Mexico and Valhall field in the North Sea where $S_{h\min}$ magnitudes calculated by frictional faulting equilibrium accurately predict measured magnitudes of the least principal stress.

3.2 Stress predictions from elastic loading models

For over 40 years, the approach originally proposed by Eaton (1969) has been used and adapted by many researchers to predict continuous variations of stress magnitude with depth. As mentioned above, he developed this relation in the context of the Gulf of Mexico in order to estimate the magnitude of S_{hmin} to define the

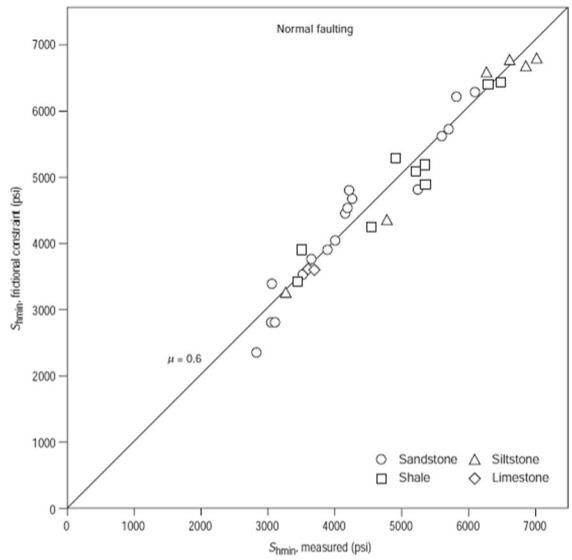

Fig. 6 The estimated values of S_{hmin} from Eq. 1 for a normal faulting regime as compared with measured stress measurements in five wells drilled in the Cotton Valley and Travis Peak formations in east Texas (from Zoback 2007). The stress measurements are consistent with the predicted stress values by frictional faulting equilibrium, thus demonstrating that the state of stress was in a state of frictional faulting equilibrium as predicted by Eq. 1

maximum mud weight so as not to accidentally hydraulically fracture a formation during drilling. Eaton's method was derived assuming that the only source of horizontal stress is the gravitational load which is instantaneously applied to a layered elastic rock. When the vertical stress is applied to a formation with lateral confinement (no horizontal strain), the formation also experiences an increase in horizontal stress, S_h, which would be equal in all directions. Based on linear elasticity, this relation between increase in vertical and horizontal stresses was proposed by Eaton to be:

$$S_h = \frac{v}{1-v}\left(S_V - P_p\right) + P_p \tag{2}$$

where P_p is pore pressure and v is the Poisson's ratio in an isotropic and homogeneous elastic medium. Therefore, if pore pressure is known and S_V and v are determined from density and sonic logs, a profile of horizontal stress S_h with depth can be obtained. Eaton (1969) recognized that Eq. 2 provided a good fit to available measurements in the Gulf of Mexico at relatively shallow depth where pore pressure was hydrostatic. However, he also showed that it was necessary to use an empirically-determined and a depth-dependent Poisson's ratio that increased to unreasonably high values approaching 0.5 at depths with severe overpressure. It is an interesting coincidence that when pore pressure is hydrostatic, Poisson's ratio is ~ 0.25 and the coefficient of friction is ~ 0.6, Eqs. 1 and 2 predict essentially the same value of S_{hmin}. In other words, Eaton's observations that Eq. 2 appears to be valid in the Gulf of Mexico, an area characterized by normal faulting, when pore pressure is hydrostatic equally could have been taken as support for the applicability of Eq. 1.

As discussed at greater length by Zoback (2007), there are two fundamental shortcomings of the assumptions inherent to the model described by Eq. 2. First, in geologic environments like the Gulf of Mexico, sediments are being deposited in a subsiding basin with an overburden load that increases with time. Initially, the increasing weight of the overburden is acting on very weak sediments that will, over time, undergo compaction and diagenesis with burial. At some point the sediments may eventually become reasonably represented as a linearly elastic solid. Thus, the assumption of an instantaneously applied vertical stress to a formation with present-day elastic properties at a given depth is not an accurate representation of how stress accumulates over time. Over the years, many cases studies have shown that direct measurements of S_{hmin} are not consistent with this simple model. In the Paris basin, minimum horizontal stress magnitudes were found to be larger within the clay-rich than that in the adjacent limestone (Gunzburger and Cornet 2007) analogous with the cases illustrated in Figs. 1–3. McCormack et al., (2023) show measured values of the least principal stress essentially equivalent to the overburden stress in southern Colorado, an area characterized by normal faulting.

Equally important is the fact that tectonic processes also contribute to the horizontal stresses such that S_{hmin} and S_{Hmax} are almost never equal (Zoback and Zoback 1980; Zoback et al. 1989). Equation 2 predicts the horizontal stress in the earth to be equal and less than S_V but it has been known since Anderson (1939), and well-documented for over 50 years, that the magnitude of S_{Hmax} exceeds S_V in strike-slip faulting areas ($S_{Hmax} \geq S_V \geq S_{hmin}$) and both horizontal principal stresses exceed S_V in reverse faulting environments ($S_{Hmax} \geq S_{hmin} \geq S_v$).

To overcome some of the shortcomings of assumptions associated with Eq. 2, various modifications have been proposed. For example, based on a plane-strain model in a linearly elastic, layered earth, Blanton and Olson (1999) proposed adding instantaneously applied horizontal tectonic strains (in orthogonal, horizontal x and y directions) as a function of depth:

$$\sigma_{hx} = \frac{v}{1-v}\left(S_V - \alpha_p\right) + \alpha_p P_p + \left[\epsilon_x + v\epsilon_y + (1+v)\alpha_T \Delta T\right]\frac{E}{1-v^2} \tag{3}$$

$$\sigma_{hy} = \frac{v}{1-v}\left(S_V - \alpha_p P_p\right) + \alpha_p P_p + \left[\epsilon_y + v\epsilon_x + (1+v)\alpha_T \Delta T\right]\frac{E}{1-v^2} \tag{4}$$

where S_V and ν are as in Eq. (2), P_p is pore pressure, α_p is the Biot coefficient, α_T is the coefficient of thermal expansion, ΔT is the change in temperature and E is Young's modulus. ε_x and ε_y are two unknown horizontal strains acting in orthogonal directions. The horizontal principal stresses are expressed as effective stresses to account for pore pressure. In principle, one could use a suite of well logs to obtain S_V (from density), ν and E to estimate stress magnitude as a function of depth. However, one also needs to estimate values of ε_x and ε_y from limited measurements of the least principal stress available for calibration (often a DFIT test at the toe of horizontal wells or an extended leakoff test or

mini-frac at the bottom of a vertical well). It is virtually impossible to estimate α_p and α_T (which represent the Biot poroelastic coefficient and the coefficient of thermal expansion, respectively) from logs such that values need to be estimated empirically. Perhaps most importantly, this formalism also assumes both instantaneously applied overburden stress as in Eq. 2 and instantaneously applied horizontal tectonic strains. Thus, using this approach leaves one left with many parameters that are unconstrained by well logs which need to be determined empirically. Simply considering the case showing the pronounced lithology dependent variations of S_{hmin} with depth in Sect. 2, it is not clear how stress measurements at one, or a few, depths could be used to achieve an adequate calibration.

Another attempt to overcome the shortcomings of Eq. 2 was an attempt to incorporate the effects of elastic anisotropy, poroelasticity, and tectonic loading Eqs. 5 and 6 (after Thiercelin and Plumb (1994), assumes vertical transverse isotropy and horizontal tectonic loading

$$S_{\mathrm{hmin}} - \alpha P_{\mathrm{p}} = \frac{E_h}{E_v}\frac{v_v}{1-v_h}\left(S_v - \alpha P_{\mathrm{p}}\right) + \frac{E_h}{1-v_h^2}(\epsilon_h - v_h\epsilon_h) \tag{5}$$

$$S_{\mathrm{hmax}} - \alpha P_{\mathrm{p}} = \frac{E_h}{E_v}\frac{v_v}{1-v_h}\left(S_v - \alpha P_{\mathrm{p}}\right) + \frac{E_h}{1-v_h^2}(\epsilon_H - v_h\epsilon_h) \tag{6}$$

where E_v and E_h are the vertical and horizontal Young's moduli, respectively; ν_v and ν_h are the vertical and horizontal Poisson's ratio; α is Biot's coefficient; ε_H and ε_h are the tectonic strains in the direction parallel to the maximum and minimum horizontal principal stresses (S_{Hmax} and S_{hmin}). In Eq. 5, the first term is the horizontal stress due to gravitational loading (S_h) similar to Eq. 2. The second term describes the horizontal stresses arising from horizontal tectonic strains with constant strain boundary condition in the horizontal direction and constant stress boundary condition in the vertical direction. The addition of the horizontal tectonic loading allows the presence of more compressive environments ($S_h > S_v$) but to potentially explain bed-to-bed variations in horizontal stress magnitudes many calibration points would be needed, but the extrapolation of measured values to other depths would be questionable.

In summary, a fundamental shortcoming of elastic loading models is that sedimentary formations are not elastic (throughout geologic time) and the assumption that stress in these formations today results from instantaneously applied stress (and/or strain) is simplistic. In other words, these models do not acknowledge that rock deformation and stress evolve due both plastic and time-dependent processes not captured by linear elasticity. Long-term, time-dependent deformational processes are not accounted for in Eqs. 3–6 but are essential in understanding how stress magnitudes vary with depth. In practical situations, it is common for there to be very limited direct measurements of the S_{hmin} (via minifracs or DFITs), such that the many unconstrained parameters in Eqs. 3–6 result in a non-unique fit to the available data. However, in recent years, multiple case studies with multiple measurements of S_{hmin} with depth have become available, we demonstrate in Sect. 5 that elastic loading models do not reliably predict stress magnitudes.

3.3 Estimating stress magnitude from viscoplastic stress relaxation

Before discussing how the concept of viscoplastic stress relaxation (VSR) can be used to estimate the magnitude of S_{hmin}, it helpful to first review more than a decade of laboratory investigations of the time dependent deformation of samples from unconventional oil and gas reservoirs throughout the U.S. (see Sone and Zoback 2013 and an overview in Zoback and Kohli 2019). This work demonstrated that it was possible to utilize lab-determined constitutive relations to create a generalized formalism for determining variations of the magnitude of S_{hmin} with depth in oil and gas reservoirs. Stress magnitude prediction based on VSR will be discussed in Sect. 4. In this section we review the laboratory studies that justify the application of the concept of VSR for explaining lithologically-controlled stress magnitudes variations with depth in sedimentary basins shown in Sect. 1. In brief, laboratory experiments show that lithofacies with low clay + TOC have higher values of Young's modulus than lithofacies with more ductile high clay + TOC content. Thus, in terms of measurable elastic properties, the variation of the magnitude of S_{hmin} with lithology indicates a clear inverse correlation between Young's modulus and stress magnitude. The lower Young's modulus, the higher the value of S_{hmin}—the exact opposite of the predictions of elastic loading models.

Sone and Zoback (2013) showed that time dependent deformation in high clay + TOC samples could be described in terms of a simple power law similar that had been previously used for rock-like materials such as concrete:

$$S_1 - S_3 = \dot{\epsilon}\frac{1}{B}\frac{t^{1-n}}{1-n} \quad (7)$$

where S_1 and S_3 are the maximum and minimum principal stresses, $\dot{\epsilon}$ is the strain rate over recent geologic time, t (meaning the last few million years, as discussed below), B is the elastic compliance factor (basically $1/E$ where E is Young's modulus and n is the creep parameter describing how much time-dependent deformation occurs under constant loading. While, most of the viscous strain we observe in the lab is permanent, (Sone and Zoback 2013) showed that because the amount of viscous strain is quite small in the formations of interest (intraplate rocks typical of unconventional reservoir settings), and linearly proportional to the applied stress, viscoelastic theory is applicable. The formations studied in the laboratory by had varying amounts of clay and kerogen content. As one might expect, they observed more viscoplastic deformation in rocks with high clay+TOC. However, even over tens of millions of years, viscoplastic strains of less than 1% are expected because the creep constitutive law that provides the basis for Eq. 7 predicts rapidly decreasing strain rates with time (see Fig. 3–14 in Zoback and Kohli 2019). Laboratory studies by Rassouli and Zoback (2018) showed that some carbonate rich unconventional reservoir formations also exhibit significant amounts of viscoplastic deformation. Zoback and Kohli (2019) compile the results of a number of studies of the physical (including viscoplastic) properties of sample with varied compositions from unconventional formations in North America. Yan et al. 2023 present more recent laboratory data emphasizing variations in properties as a function of mineralogy and heterogeneity.

Figure 7a illustrates some of the laboratory tests where strain is measured as a cylindrical rock sample is loaded and unloaded axially at stress levels much too small to damage the sample. Note that as loads are applied, there is both elastic and viscous deformation. Analysis of the viscous deformation in the context of the best fitting constitutive law (Eq. 7) allows B and n to be determined in the manner illustrated in Fig. 7b. The viscous deformation plotted in log–log space yields n from the slope of the line and B from the intercept. As shown in Fig. 7c, whether a particular formation tends to exhibit a great deal of viscoplastic deformation (such as the Haynesville and Eagleford) or relatively little (such as the Barnett) there is a clear increase in **n** as stiffness decreases. Figure 7d illustrates that, from a geological perspective, VSR happens very quickly. In other words, for a relatively high value of "n" (0.06, for example), 90% stress relaxation is expected over 200 million years. However, more than 80% of stress relaxation occurs after only 1 million years. Thus, the stress state "re-sets" as large-scale geological processes associated with relative plate motions typically act over time periods of 10's of million years. Two obvious examples are the current tectonics of the western U.S. associated with evolution of the San Andreas Fault system and related Basin and Range/Rio Grande Rift provinces as well as the Gulf of Mexico sedimentary basin. Thus, changes of the state of stress (and associated strain) reflect processes active over the past few million years.

There are two important aspects of the constitutive law for VSR that will enable its use for stress magnitude determination in Sect. 5. First, the total amount of stress relaxation occurs over relatively short periods of geologic time. As shown in Fig. 5d (after Ma and Zoback 2020), for a given value of n, essentially all the stress relaxation occurs in about 1 million years. The means that as tectonic process change in an area (for example, from compression to extension) over periods of millions of years, the stress changes resulting from VSR, essentially "reset" along with the regional stress state. Note also that for relatively high values of n, essentially complete stress relaxation can occur, meaning that all three principal stresses essentially equal. This seems to explain the measurements of $S_{hmin} \approx S_V$ shown in Sect. 2 as well as the results reported by Gunzburger and Cornet 2007 and McCormack et al. 2023. In fact, laboratory experiments done in the latter study established that n values in excess of 0.1, imply complete stress relaxation (Fig. 7d). Second, Sone and Zoback (2014b) showed that it is not necessary to "track" VSR throughout a rock's history and the terms representing strain rate and time in Eq. 7 can be considered as "total strain", independent of the time evolution of strain, which is empirically determined. This greatly facilitates calibration of the VSR method for stress prediction, as shown below.

4 Utilizing VSR to determine S_{hmin} as a function of depth

Figure 8 (after Zoback and Kohli 2019) represents a conceptual representation of an alternating sandstone and shale formations in a normal/strike slip faulting environment ($S_V \approx S_{Hmax} \geq S_{hmin}$). When relatively

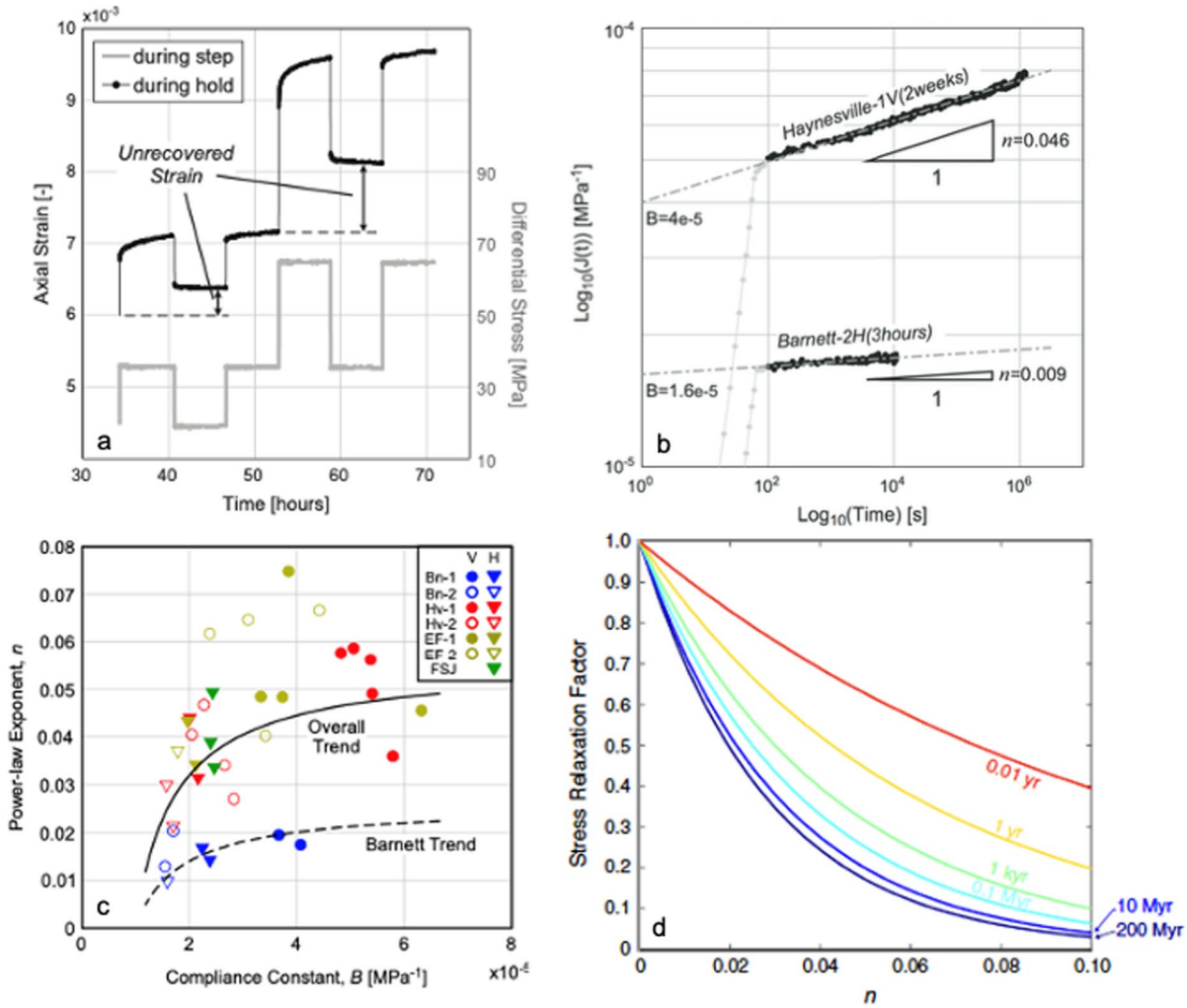

Fig. 7 **a** Axial strain as a function time in a step loading/unloading experiment on a cylindrical sample subjected to a constant confining press. The axial load is shown in gray, the measured strain in black (REF). **b** Plotting the viscoplastic strain in log–log space allows n and B to be determined from the slop and intercept respectively (Sone reference). **c** All clay and kerogen containing samples show increasing viscoplastic strain as expressed by the parameter n as the compliance increases, meaning that n increases as Young's modulus decreases (Figs. 6a,b,c from Sone and Zoback 2013). **d** The degree of stress relaxation is a function of n and time. As shown by Ma and Zoback (2020), low values of n result in little stress relaxation whereas high values of n can lead to near complete stress relaxation. In terms of geologic time, stress relaxation occurs quite rapidly, on the order of 1 million years (see text)

stiff rocks (*e.g.*, sandstone layers) are in frictional equilibrium, Eq. 1 predicts magnitudes for S_{hmin} being equal to about 60% of the vertical stress for hydrostatic pore pressure and a coefficient of friction of 0.6 (see also Fig. 5h). This is shown as function of depth in Fig. 8 and is illustrated by the Mohr diagram (note that the *x*-axis is total stress, not effective stress in this representation). Assuming that the shales exhibit some degree of stress relaxation, the least principal stress would be expected to be higher in the shales as illustrated for the layers above and below the sandstone layer. This is illustrated by the smaller Mohr circles, depending on the degree of stress relaxation and corresponding increase in S_{hmin}. This schematic diagram is a simplified representation of the correlation between the magnitude of S_{hmin} and clay + TOC shown in Figs. 1, and 3. If one were carrying out hydraulic fracturing operations in the upper sand, the

moderately higher stress in the overlaying shale provides a moderate barrier to upward propagation. As long as the pressure during hydraulic fracturing in the sand did not exceed the least principal stress in the overlaying shale, the hydraulic fracture propagation would not propagate upward out of the sand layer. The shale below, however, is a more significant stress barrier, reflecting a greater degree of viscoplastic stress relaxation. Conversely, if one were hydraulically fracturing the clay and organic rich shales and mudstones (as is the case in unconventional oil and gas development), hydraulic fracture propagation into adjacent sands is difficult to constrain.

In this section we first discuss the concept of VSR affecting S_{hmin} magnitudes as a heuristic model that allows us to make inferences about relative changes of the magnitude of S_{hmin} with depth based on changing lithology. We then show several examples in which VSR can been used making case-dependent empirical correlations to create a continuous estimate of S_{hmin} magnitudes with depth. With multiple measurements of S_{hmin} in different lithologies, we first establish a correlation between S_{hmin} and lithology. Second, we use geophysical logging data to create an empirical correlation between Young's modulus and n. Finally, we consider a mathematical formalism that allows for detailed predictions of stress magnitude with depth when there are fine scale variations of lithology with depth. A requirement of this formalism, however, is that there is a number of direct measurements of S_{hmin} with depth for calibration. As will be demonstrated in Sect. 5, fine scale variations of stress magnitude can have a profound effect on hydraulic fracture growth, depending on the exact depth where individual stages in a horizontal well are located with respect to the lithologically-controlled variations of stress magnitude.

4.1 *Qualitative use of VSR for estimating S_{hmin} variations with depth*

Based on the principle of VSR, Sone and Zoback (2014a) interpreted the variation of the occurrence of wellbore failures (wellbore breakouts and drilling induced tensile fractures) in terms of variations of the stress concentration around the wall of a vertical well. As the magnitude of S_{Hmax} increases, so does the likelihood of wellbore breakouts, similarly as the difference between S_{Hmax} and S_{hmin} increases, so does the likelihood of inducing drilling-induced tensile fractures. Thus, the absence of wellbore failures in clay-rich formations could be directly related to lithology in terms of their being less stress anisotropy in those formations due to VSR.

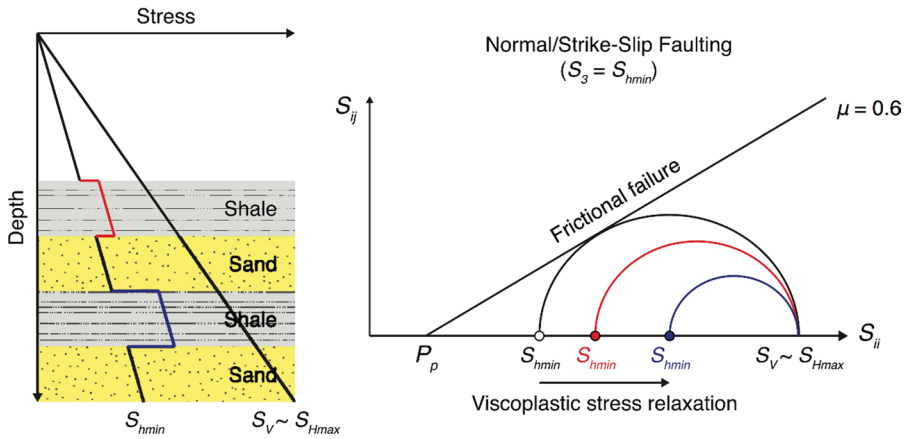

Fig. 8 Schematic diagram illustrating how viscoelastic stress relaxation results in decreasing stress anisotropy due to increasing the magnitude of the least principal stress (after Zoback and Kohli 2019) representative of a strike-slip/normal stress state as illustrated in Fig. 5b ($S_V \approx S_{\text{Hmax}} \geq S_{\text{hmin}}$). The simplified cross-section on the left shows the least principal stress in the sands being consistent with frictionl equilibrium (as illustrated by the Mohr circle shown with a black line). A moderate increase in the magnitude of the least principal stress above the upper sand results from a minor amount of viscoplastic stress relaxation whereas a greater amount of stress relaxation in the shale below the sand creates a larger stress difference and thus a more effective barrier to vertical fracture growth

Figure 1 showed lithologically-controlled variations of S_{hmin} with depth at the HFTS-1 Midland Basin (Kohli and Zoback 2021). There were an unusually large number of stress measurements at different depths that allowed Kohli and Zoback to create an estimated profile of stress magnitudes with depth that match the stress measurements in a manner consistent with the lithology changes. The dotted line in Fig. 1 is (replicated and simplified in Fig. 9a, from Kohli and Zoback 2021) are inferences about stress magnitude based on lithology, even though there were no measurements at a number of depth intervals of interest. Despite this somewhat qualitative nature of the estimated stress variations with depth, Fig. 9 illustrates the value of understanding stress variations with depth to better understand of the reservoir stimulation process. For example, two stages in one well (Figs. 9b,c) exhibited markedly different microseismic responses to hydraulic fracturing. The stage near the toe of the well showed no microseismic events until about 1.5 h after pumping began (Fig. 9b). This is apparently due to the initial value of S_{hmin} being very high due to the stage being in a clay-rich lithofacies and the initial state of stress not being in frictional equilibrium (Fig. 9c). Thus, significant pressure build-up during the hydraulic fracturing stage is required before slip on pre-existing faults could occur. In marked contrast, Fig. 9d shows results from a stage close to the heel of the well is in a lithofacies which has a much lower value of S_{hmin} (due to relatively low clay + TOC) that is much closer to the value predicted by frictional faulting (Fig. 9e). Thus, microseismic events begin as soon as pumping begins as only minimal pressure changes in the formation surrounding the hydraulic fracture. Finally, Kohli and Zoback demonstrated that the planes on which slip occur during a stage near the middle of the same well are directly explainable in terms of the stress state and an increase in pressure in the formation occurs with time (Fig. 9f).

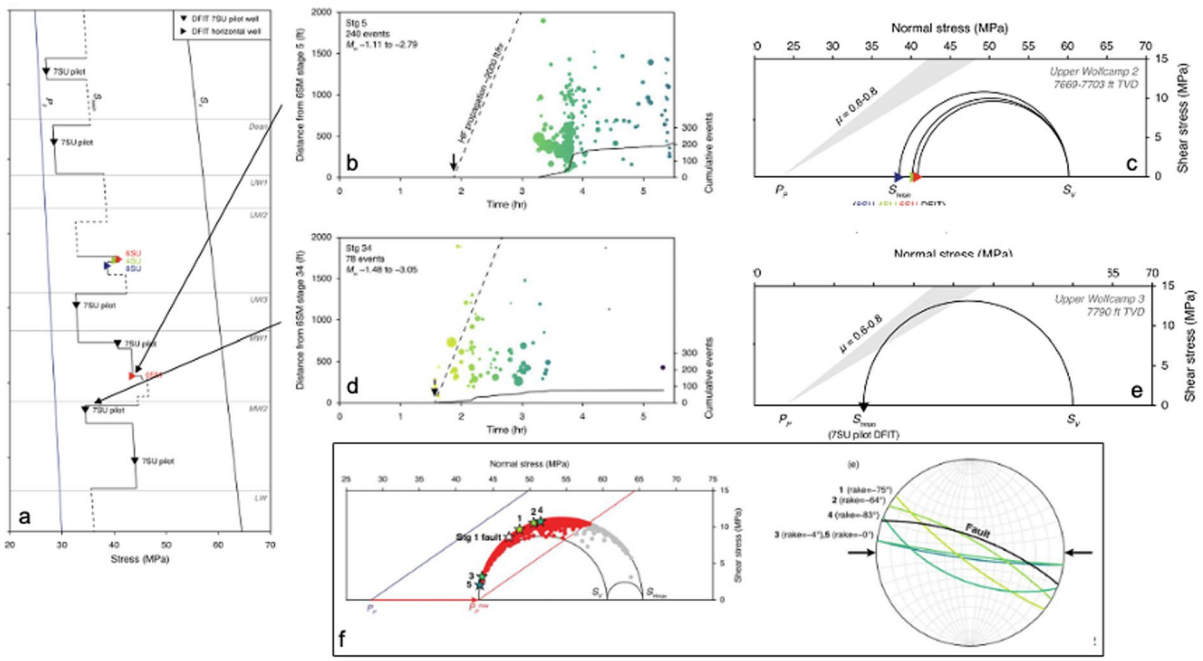

Fig. 9 **a** Measured values of the S_{hmin} as a function of depth in the HFTS-1 wells. **b** The development of microseismic events as a function of distance from a stage near the toe of the well with time. Note that no microseismic events occur until about 1.5 h after pumping begins. The diagonal line represents a hypothetical expansion of microseismic events with time. **c** The magnitude of S_{hmin} with the stage shown in (b) is not in frictional equilibrium due to VSR. **d** Microseismic events in a stage closer to the heel of the well begin immediately and spread out from the well. **e** S_{hmin} low in this stage (because of low clay) resulting in a state of stress in frictional equilibrium. **f** A representation of slip on faults of various orientations in a stage in the middle of the same well is directly explainable in terms of the initial state of stress and the evolution of pressure over time. All figures are from Kohli and Zoback (2021)

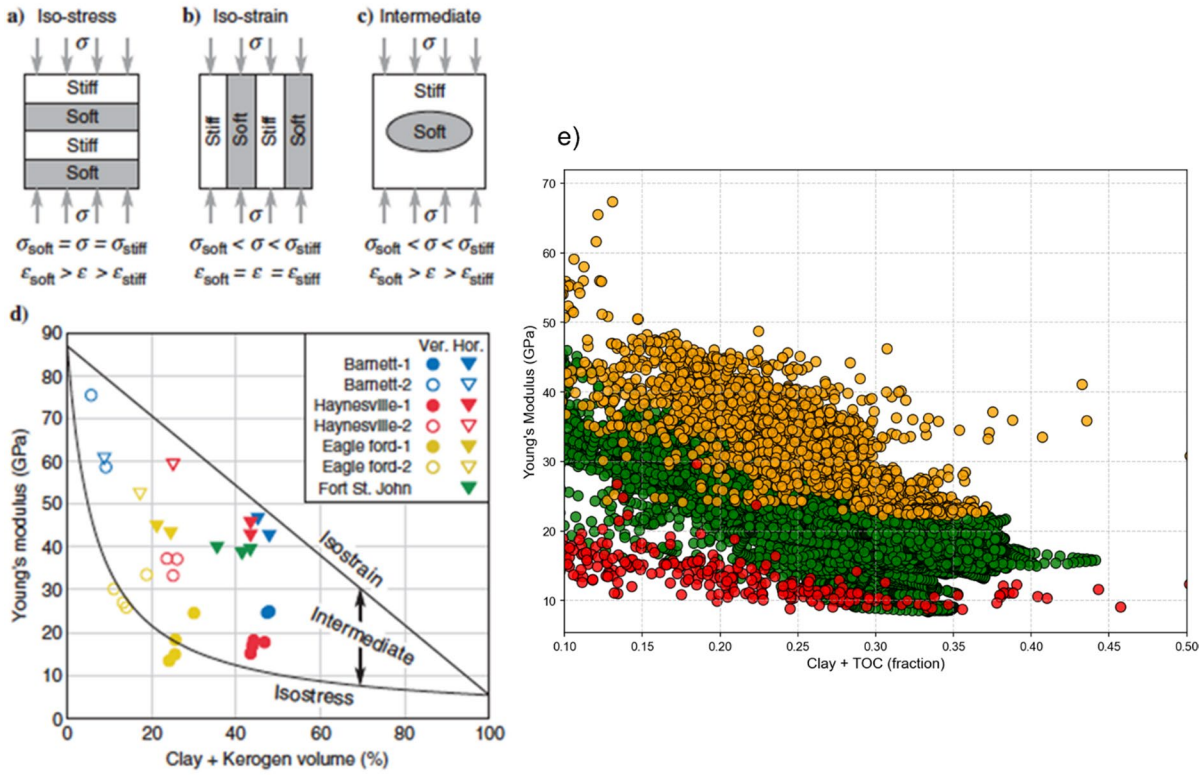

Fig. 10 **a** Schematic of a layered shale model loaded perpendicular to the bedding, representing the isostress condition. **b** Schematic of a layered shale models loaded parallel to the bedding, representing the isostrain condition. **c** An example of shale models that could result in an intermediate state between isostress and isostrain. **d** Laboratory Young's modulus data plotted against the sum of clay and kerogen volume, together with the Voigt and Reuss bounds calculated assuming Esoft. 5.4 GPa, Estiff 86.9 GPa (from Sone and Zoback (2013). **e** The relationship between Young's modulus and clay plus TOC volume determined from well log data in three wells. The red dots are for the HFTS-1 well. The green dots are for the proprietary data set utilized by Singh and Zoback (2022) that is discussed below. The orange dots are for a proprietary data set in Canada

4.2 *Empirical correlations for estimating S_{hmin} variations with depth*

As introduced in discussion of Fig. 6, extensive laboratory tests using samples from unconventional oil and gas reservoirs showed that the degree of viscoplastic deformation depended on the concentration of soft minerals (clay plus organic content) as indicated by the correlation of the viscoplastic parameter n in Eq. 5 with clay + TOC. Looking ahead to applications utilizing standard suites of geophysical well logs, it is preferable to utilize Young's modulus as a metric rather than the mass fraction of clay + TOC. This is why we parameterized the constitutive law presented in Eq. 7 in terms of Young's modulus.

One of the initial findings of the laboratory experiments reported by Sone and Zoback (2013) was that creep compliance (strain normalized by applied stress) was greater in the bedding-perpendicular direction than in the bedding-parallel direction. To explain this observation, they refer to a simple model in which an anisotropic gas shale rock is represented by a composite of soft and stiff layers (Fig. 10a and b). Soft layers represented by clay and kerogen content, and stiff layers represent other minerals such as quartz, feldspars, and carbonates. We then examine the stresses carried by each layer when a far-field uniaxial stress σ is applied to the rock. Here, they simplified the problem to one-dimension, treating stress, strain, and stiffness as scalar values. Thus, the layer properties are mechanically isotropic, and

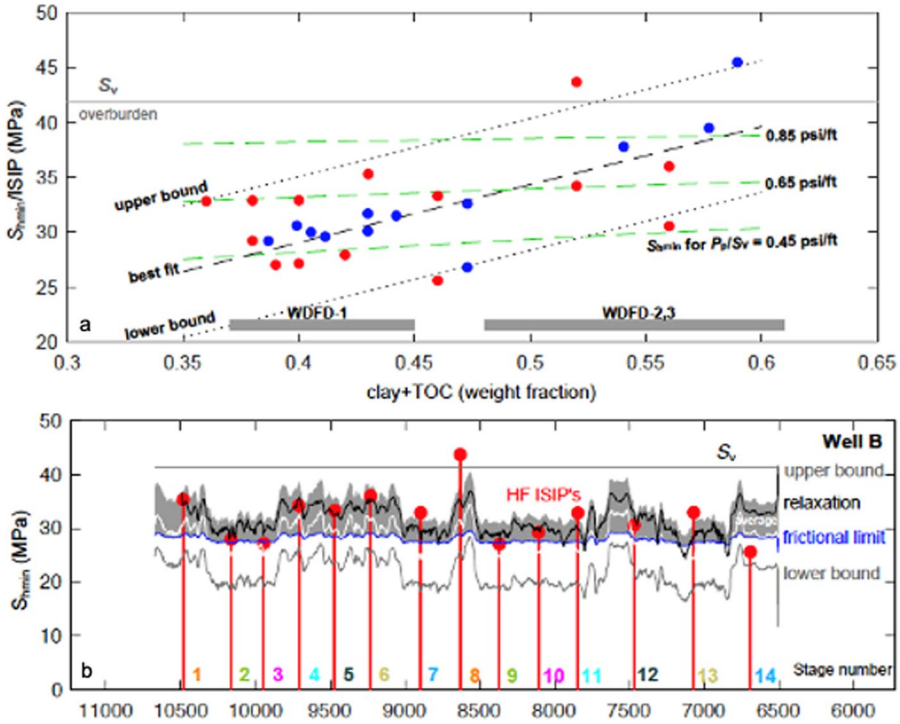

Fig. 11 **a** Variation of S_{hmin} estimated from stage ISIPs as a function of clay plus TOC shows an overall positive trend and most of the stages fall within the bounds described in the study. **b** The ISIPs for Well B (previously shown in Fig. 2) show consistent agreement with the stress profile obtained by using the empirical correlation for the *n* parameter (from Ma and Zoback 2020)

shear tractions at the layer boundaries are ignored. When the far-field stress is loaded perpendicularly to the layers (Fig. 10a), it represented a sample in the lab loaded perpendicular to bedding, this is an isostress condition in which the stresses carried by each layer are essentially the same as the far-field stress. In this case, the average stiffness of the whole rock is the Reuss (harmonic) average of the stiffness of each layer. When the loading direction was parallel to the layers (Fig. 10b), it corresponded to an isostrain condition the average stiffness of the whole rock and equal to the Voigt (arithmetic) average of each layer stiffness. Because the Voigt average is greater than the Reuss average, we note that as expected, samples loaded parallel to bedding are elastically stiffer than those loaded normal to bedding. Note in Fig. 10d that Young's modulus decreases with increased clay + TOC content and that the tests carried out in an iso-strain geometry (axial loading was parallel to bedding shown by the inverted triangles) the stiffness is greater than when loaded perpendicular to the bedding (circular symbols). Other variations between different samples likely results from factors such as clay mineralogy, digenesis and fabric.

Figure 10e shows the correlation between Young's modulus and Clay + TOC for three vertical wells. The green dots are for the proprietary data set from the Midland Basin that was utilized by Singh and Zoback (2022) and discussed below. The red dots are for the HFTS-1 well introduced in Fig. 1. The orange dots are data from a proprietary set in Canada. Note that in each case, there is a clear, inverse relationship between Young's modulus and clay + TOC for field data. In fact, while there is a significant variation in overall stiffness in these three sets of data, in each case the measured values of E_{vert} are about half the value when clay + TOC is about 30%, compared with the values when it is

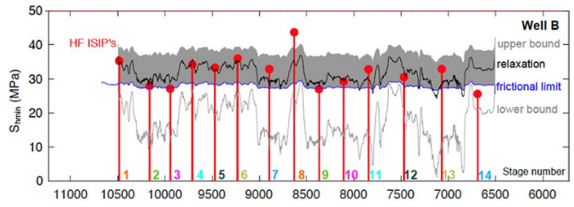

Fig. 12 The predicted stress magnitudes (black line) fit the measured data reasonably well. As was the case Fig. 9, the frictional constraint provides a meaningful lower bound for estimated values of S_{hmin} (from Ma and Zoback 2020)

about 10%. In these datasets we have highlighted data points with at least 10% clay + TOC to show its impact on stiffness. For zones with less than 10% clay + TOC the stiffness is affected significantly by presence of small quantities of heavy minerals like pyrite.

In general, to apply Eq. 7 for estimation of S_{hmin}, we are principally interested in Young's modulus parallel to bedding (E_{horiz}). Thus, if Young's modulus is determined from geophysical logs in a vertical well, it will be determining Young's modulus normal to bedding (E_{vert}), a lower value than had it been measured in a horizontal well. Converting from E_{vert} to E_{horiz} in the context of implementing VSR was discussed by Singh and Zoback (2022) which is reviewed below.

Figure 11a (from Ma and Zoback 2020) shows an empirical correlation between the measured values of S_{hmin} and the log-determined values of clay + TOC (for the well previously shown in Fig. 2) using logs run in the horizontal wells. Note in Fig. 11b that the correlation between the range of predicted values of S_{hmin} compares reasonably well with the measured values. The stages with ISIP values higher than the overburden stress correspond to the stages where the well landed in high clay + TOC lithofacies. The black line in Fig. 11b indicates the best fitting line in Fig. 11a. In gray, we show the bounds of the predicted values of S_{hmin} incorporating the upper bound of uncertainties in the correlation in Fig. 11a and a lower bound provided by frictional constraints (blue line) assuming only that the vertical stress, S_V, is the largest stress and pore pressure. The lower bound of S_{hmin} predicted from the correlation shown in Fig. 11a turns out to be irrelevant. Correlations such as that shown in Fig. 11a may or may not be practical in many cases. In this case, the two wells were very close to one another such that variables such as depth (S_V), pore pressure and lithology were irrelevant. Equally important is that because this is a strike-slip/normal faulting area ($S_V \approx S_{Hmax} \geq S_{hmin}$ as illustrated in Fig. 5b), the lower bound of stress magnitude could be predicted using Eq. 1 and the upper bound was obviously S_V.

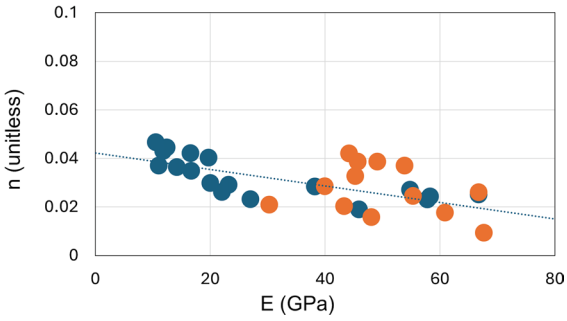

Fig. 13 Empirical correlation for n as a function of Young's modulus that includes the data of Ma and Zoback (2020) shown by the red dots with more recent data from Mandal et al. (2021) shown by the blue dots

Utilizing the VSR formulation in Eq. 7 and the equivalence of the parameter B as the reciprocal of the Young's Modulus E, (Sone and Zoback 2013) we can re-write the expression for S_{hmin} as:

$$S_{hmin} = S_V - \dot{\epsilon} E_{horz} \frac{t^{1-n}}{1-n} \tag{8}$$

The horizontal Young's modulus (E_{horz}) can be computed from sonic log data in a vertical well (which would yield E_{vert}) utilizing methods described by Singh and Zoback (2022) and summarized below. As shown in Fig. 5d, whenever the predicted amount of stress relaxation is non-trivial (corresponding to all values of n greater than about 0.01) any amount of time more than one million years could be used in Eq. 8 resulting in little uncertainty in the amount of stress relaxation expected to occur.

While the viscoelastic parameter n can be determined experimentally in the laboratory, this is not practical in most applications. Ma and Zoback (2020) derived an approximate empirical correlation between the lab derived horizontal Young's modulus and the parameter n using laboratory values available at that time. Figure 12 shows a comparison between the measured values of S_{hmin} and the range of predicted values using these correlations for the same well shown in Figs. 2 and 11. As in Fig. 11b, the S_{hmin} was highest when a frac stage was in high clay and TOC lithofacies. Again, the black line indicates the best fitting line and gray represents the bounds of the predicted values of S_{hmin} incorporating an upper bound of uncertainties in the correlation and a lower bound provided by frictional constraints (blue line) assuming that the vertical stress, S_V, is the largest stress. Again, the lower bound of S_{hmin} based on the empirical correlation between E and n turns out to be irrelevant.

Figure 13 shows an improved correlation between n and the parameter E that includes data from both

Ma and Zoback (2020) and Mandal et al. (2021). The latter study carried out laboratory experiments similar to those included in the Ma and Zoback (2020) study. The best-fitting straight line in Fig. 13 can described by the following equation:

$$n = .042 - 0.0003E \tag{9}$$

(where E is in units of GPa) is essentially the same as that used by Ma and Zoback (2020) and used for the stress magnitude prediction in Fig. 12. In the Ma and. Zoback study, the laboratory samples came from seven different unconventional plays in North America. Thus, they represent a wide range of lithologies and diagenetic histories as described in Zoback and Kohli (2019). The Mandal et al. (2021) samples are from the Goldwyer Formation in the Perth Basin of Australia. Clay and TOC vary by more than a factor of 10 in the samples studied. Thus, the Mandal et al. (2021) data set includes tests on a number of samples with $n \geq 0.04$ and lower values of Young's modulus. Such values correspond to formations in which appreciable stress relaxation is expected, as predicted by the calculations shown in Fig. 7d for formations characterized by relatively high n. The occurrence of cases in which there appears to be complete stress relaxation (Figs. 2, 3 and 4) would appear to be associated with even higher values of n (Fig. 7d) and lower values of E. We are aware of no reported laboratory tests on such samples.

4.3 *Estimating S_{hmin} with multiple calibration points*

In this section we present a more precise method to predict the variation of S_{hmin} with depth for a field in the Midland Basin, following Singh and Zoback (2022). The Permian basin is generally characterized by normal/strike-slip faulting stress regime, $S_V \approx S_{Hmax} > S_{hmin}$ (Snee and Zoback, 2018) illustrated in Fig. 5b. In principle, however, one could generalize this framework to estimation of S_{Hmax} as the stress relaxation of the two principal horizontal stresses would be proportional to each other. It

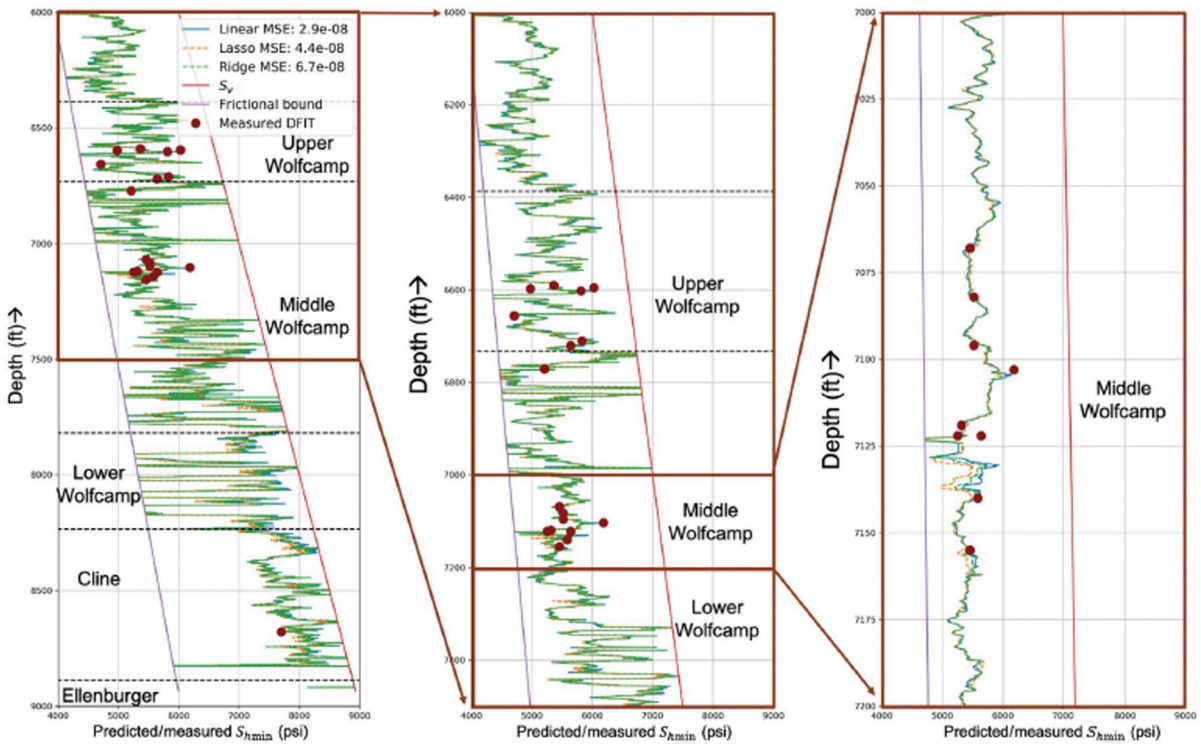

Fig. 14 Stress profiles in a field in the Midland Basin computed by Singh and Zoback 2022 using the VSR methodology parametrized by a statistical learning model. Details are provided in the text

is reasonable to assume that behavior of shales can be approximated with a vertical transverse isotropic (VTI) model (Vernik and Liu 1997). Using this formulation, we can re-write Eq. 7 as:

$$\kappa\left(S_V - S_{\text{hmin}}\right) = \dot{\epsilon} E_{\text{horz}} \frac{t^{-n}}{1-n} \tag{10}$$

where $\kappa = 1$ for normal faulting and $\kappa \leq 1$ for strike-slip faulting stress state. Therefore, the difference between S_V and S_{hmin} can be expressed as:

$$S_V - S_{\text{hmin}} = \dot{\epsilon} \frac{t^{-n}}{\kappa(1-n)} E_{\text{horz}} \tag{11}$$

As S_V at any depth can be estimated by simply integrating the weight of the overburden, we can use Eq. 10 to estimate S_{hmin} at any depth, if we can estimate the right-hand side parameters. E_{horz} can be computed from cross dipole sonic logs by assuming a vertical transversely isotropic (VTI) medium, which enables estimation of the Thomsen parameters (Thomsen 1986) either by using the Stoneley wave slowness (Walsh et al. 2006) or by using the ANNIE model assumptions described by (Murphy et al. 2015). Sone and Zoback (2015) showed that the amount of viscous stress relaxation principally depends on the amount of viscous strain that has occurred, not the manner in which the strain evolved over time. Thus, the formations of interest in this study can be assumed to have experienced similar total amounts of strain over the past few million years, which makes calibration of the VSR model much easier.

To implement the VSR concept for prediction of S_{hmin} as a function of depth using well logs from near-vertical wells, Singh and Zoback (2022) begin by determination of the creep parameter n as a function of depth z. Re-writing Eq. 10 by combining all the terms other than E_{horz} on the right-hand side into one unknown: $n^*_{\epsilon t}$, we get:

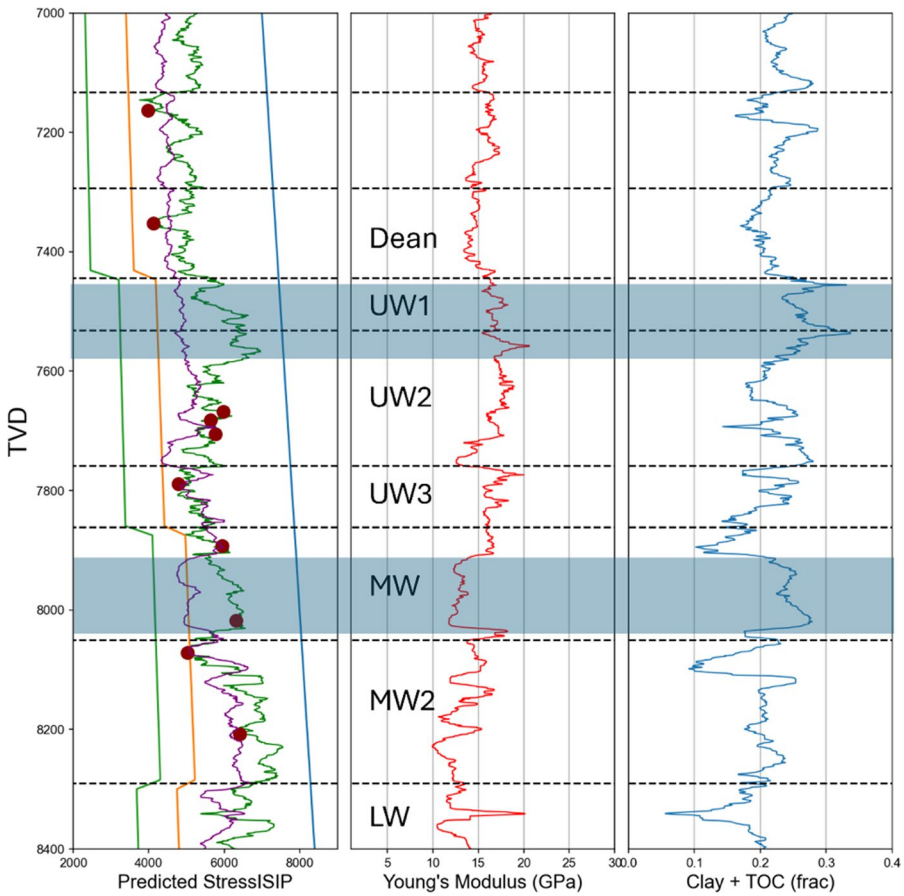

Fig. 15 The stress profile for the HFTS-1 data previously introduced in Fig. 1. Only DFIT stress measurements are shown as they were used in the calibration of the models. The straight green line represents pore pressure and the orange line represents the value of S_{hmin} predicted by Eq. 1 for a normal faulting area. The prediction using the VSR methodology (shown in green) compared with the stress profile from the extended Eaton model (shown in green). Note that the stress barriers at about 7500 and 8900 ft (as indicated by the horizontal shading) correlate well with high clay + TOC content and are completely missed by the elastic loading model

$$S_V(z) - S_{\text{hmin}}(z) = n^*_{\epsilon t}(z) E_{\text{horz}}(z) \quad (12)$$

and we can define $n^*_{\epsilon t}$ as function of the available well logs in our case study:

$$n^*_{\epsilon t} = f\left(V_{\text{clay+TOC}}, V_{\text{limestine}}, V_{\text{quartz}}, \text{GR}, \rho, \Omega, \phi\right) \quad (13)$$

where:

GR = Gamma ray log value

$V_{\text{clay+TOC}}$ = Combined volume fraction of clay minerals and total organic carbon from spectral Gamma ray log

V_{quartz} = Volume fraction of quartz from spectral Gamma ray log

$V_{limestone}$ = Combined Volume fraction of calcite and dolomite from spectral Gamma ray log

ρ = Bulk density log

ϕ = Neutron porosity log

Ω = Resistivity log

We refer readers to Singh and Zoback (2022) for a complete explanation of statistical model to fit $n^*_{\epsilon t}$ from well log data and compute a continuous stress profile. Figure 14 shows the stress profile they computed utilizing the above VSR formulation. While they had more than 20 stress measurements over a limited spatial interval in a proprietary data set from the Midland Basin, the stress profile was validated with blind tests to prevent overfitting the high number of stress measurements. These tests included bootstrap aggregation, a process by which half of the available calibration points are randomly removed, and the other half are successfully predicted. Note the strong fit of the stress profile to the input data highlighted that variations in S_{hmin} measurements which otherwise would have seemed like spatial discontinuities or random variance can in fact be explained by variation in lithological properties with depth. Even the single calibration point in the Cline formation was successfully predicted when it wasn't used in the model calibration. They also applied the same stress model in a nearby field without any additional calibration and showed a reasonable match to the stress measurements. Other cases in which VSR has

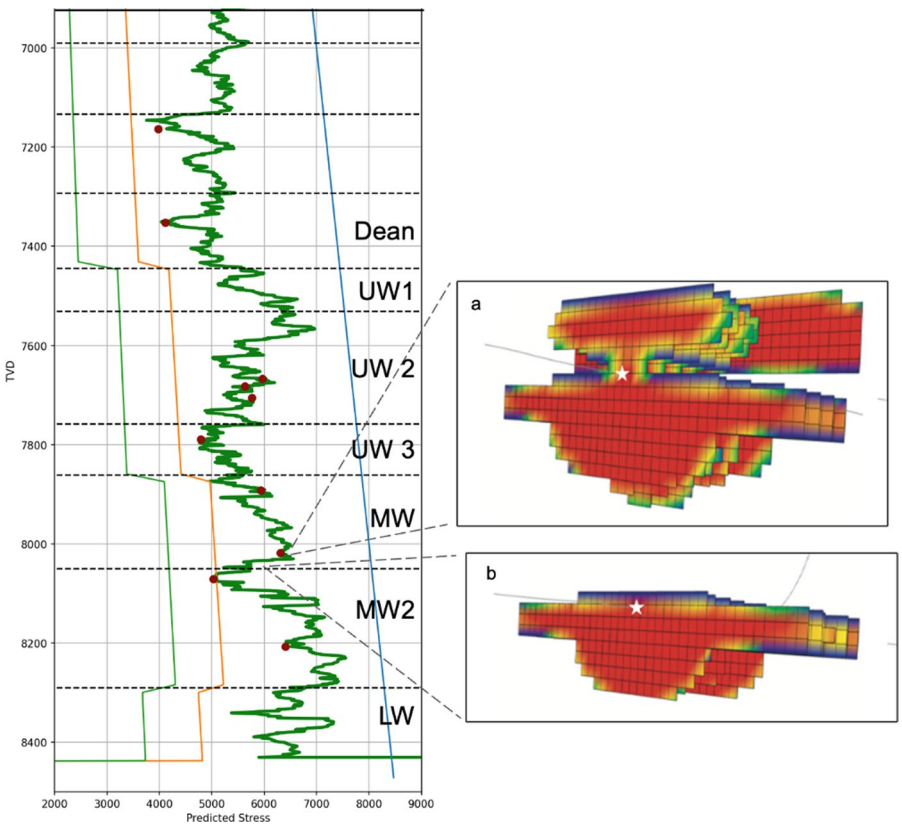

Fig. 16 A simplified representation of the variation of stress magnitude measurements and predictions in the HFTS-1 well (modified from Fig. 15). The two simulations of stages at slightly different depths (from Zoback et al., 2022) illustrate how profoundly different hydraulic fracture propagation can be for stages carried out at nearly the same depth but at markedly different magnitudes of S_{hmin} resulting from the changing lithology with depth

been used to predict stress magnitude as a function of depth are presented in Sect. 5.

4.4 Comparison of VSR and elastic loading models

Comparison of the equations describing elastic loading models (Eqs. 3–6) with that associated with VSR (Eq. 7) shows one obvious and dramatic difference. In the case of layer-to-layer variations of S_{hmin}, elastic loading models predict that S_{hmin} increases as Young's modulus increases, whereas VSR predicts S_{hmin} increases as Young's modulus decreases. Thus, as might be expected, the VSR and elastic loading models result in significantly different stress estimates in high clay plus TOC intervals due to the markedly different assumptions about how stress accumulation in the earth occurs.

Figure 15 shows a VSR stress profile for the HFTS-1 dataset utilizing the data shown in Fig. 1 and compares the results with the extended Eaton method. The VSR stress profile is obtained by utilizing the methodology from Singh and Zoback (2022). The clay content, density, Gamma Ray, carbonate content, and porosity are used to describe a fit the function described in Eq. 12. The extended Eaton model is calibrated by using the Blanton and Olson (2001) methodology from Eq. 3 and Eq. 4. The tectonic strain and Biot coefficient are modified to get a better match to the measured S_{hmin} values. As shown in the left panel of Fig. 15, the VSR methodology (green line) does a significantly better job at predicting stress variations compared to the extended Eaton model using Eq. 5 (purple line). The two measurements in the Dean (and the depths of the other low clay + TOC intervals) are reasonably well fit by Eq. 1 and illustrated schematically in Fig. 8. However, the logs show that at the depths of the relatively high S_{hmin} values are associated with low Young's modulus and high clay + TOC, as expected in the context of VSR. The shaded areas at depths of approximately 7500 ft and 7900 indicate significant barriers (1000–2000 psi) to vertical hydraulic fracture growth that are not predicted by the elastic loading model. While using the extended Eaton model, it is common practice in the oil and gas industry to match the computed S_{hmin} magnitudes at specific depths using different values of tectonic strain, Biot coefficient, poroelastic and/or thermal coefficients in different layers. This practice makes it difficult to have confidence in the

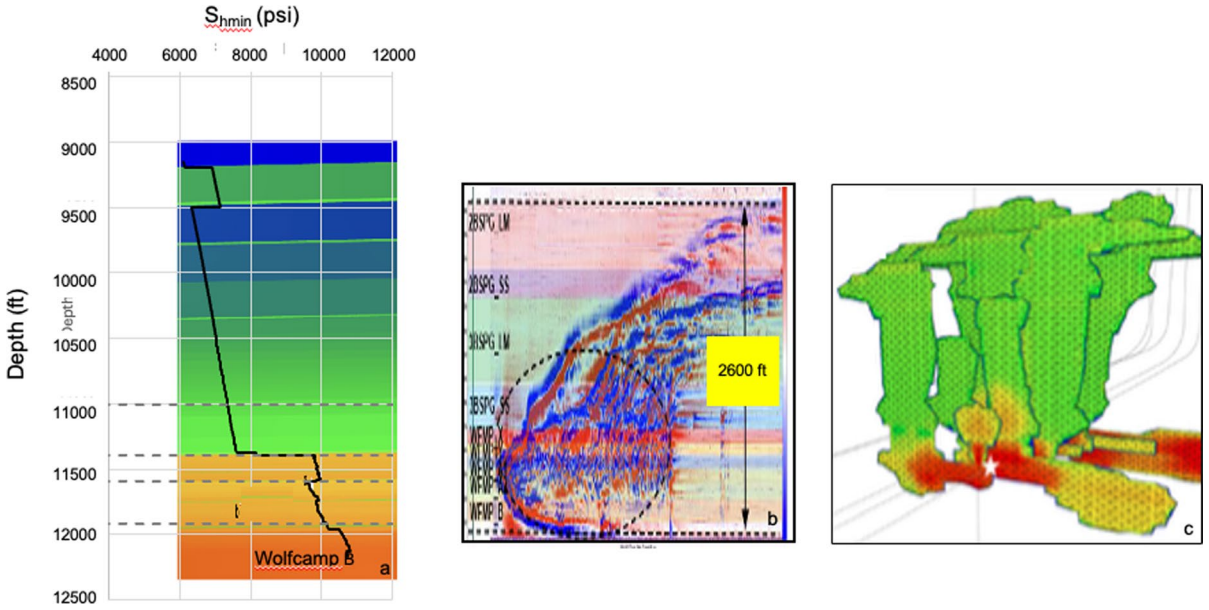

Fig. 17 **a** The stress model developed for HFTS-2 combining Eq. 1 in the low clay + TOC formations and the VSR technique in the higher clay + TOC formations, with warmer colors representing higher values of S_{hmin}. **b** Optical fiber data in vertical well R5PH) shows clear evidence of ~ 2600 ft of upward hydraulic fracture growth (from Pudugramam et al., 2022). **c** Modeled hydraulic fracture growth and proppant placement (as indicated by color) (after Zoback et al., 2022)

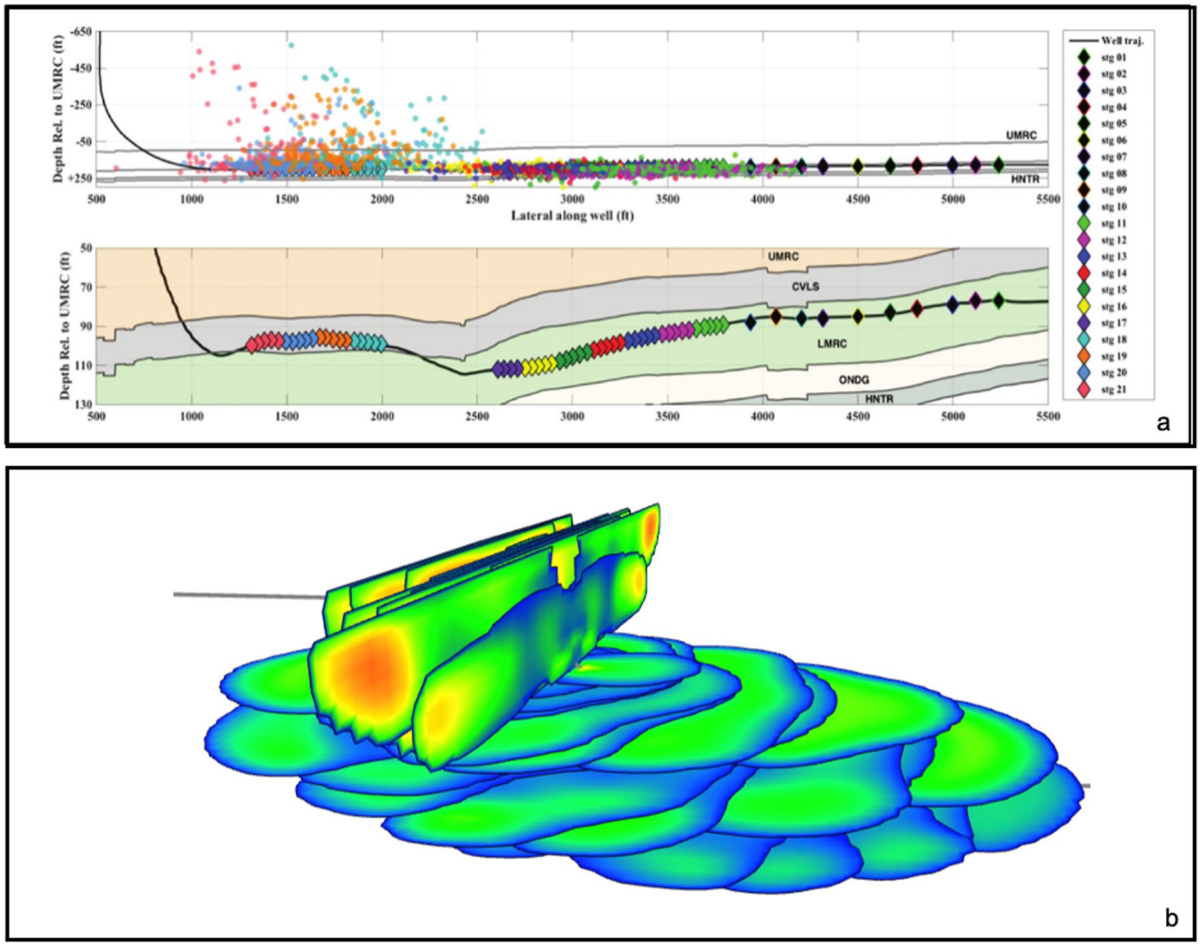

Fig. 18 **a** The top panel is a well in the Marcellus formation previously shown in Fig. 7. From Alalli and Zoback (2018). **b** Simulation of hydraulic fracture propagation in a well similar to that shown. Horizontal hydraulic fracture propagation occurs in the lower lithofacies where the three principal stresses are approximately equal due to VSR whereas vertical hydraulic fracture propagation occurs in the adjacent stages located in the upper lithofacies where S_{hmin} is slightly lower than S_V. From (Dontsov, et. al, 2026)

stress profiles outside the immediate zones of the stress measurements and creates excessive degrees of freedom which makes the model difficult to use and understand absent numerous calibration points (which effectively makes the model unnecessary).

Two other examples illustrating the difference in the stress predictions in relatively high clay plus TOC formations are presented in the Appendix. One is for the case study shown in Fig. 14 and previously discussed by Singh and Zoback (2022) in the Midland Basin. The other is from the DJ Basin in Colorado which was previously discussed by McCormack et al. (2021).

5 Impact of S_{hmin} variations on hydraulic fracture growth

In the sections above, Figs. 1, 2, 12, 14 and 15 all document abrupt variations of the magnitude of S_{hmin} with depth that are correlative with layer-to-layer lithologic variations. In this section, we demonstrate the impact of these stress variations with depth on vertical and hydraulic fracture propagation. The left panel of Fig. 16 shows a simplified version of the observed and predicted magnitude of S_{hmin} with depth in the HFTS-1 wells previously shown in Fig. 15. Following Zoback et al. (2022), we show simulations of two hydraulic fracturing stages at

slightly different depths. Each simulation attempted to replicate the frac stages that were carried out at these depths. The color represents the aperture of the hydraulic fractures after completion of the stage and thus represents the distribution of proppant in the hydraulic fractures. The simulation in Fig. 16a, corresponds to a stage with the landing zone near the bottom of MW layer where the magnitude of S_{hmin} is relatively high. The simulation shown in Fig. 16b corresponds to a stage at a slightly deeper depth, but where the magnitude of S_{hmin} is almost 1000 psi lower. Note that in case of Fig. 16a, the variation of S_{hmin} with depth causes significant downward propagation of the hydraulic fracture as well as considerable upward propagation. In marked contrast, the stage represented in Fig. 16b shows considerable horizontal hydraulic fracture propagation at the depth of the landing zone as well as downward propagation, although not as much associated seen for a stage with S_{hmin} at slightly shallower depth. Clearly, optimization of hydraulic fracturing to improve hydrocarbon recovery (and minimize produced water production from adjacent strata), requires detailed modeling of lithologically-induced stress variations with depth followed by careful placement of landing zones and hydraulic fracturing procedures.

The HFTS-2 project (Zhao et al., 2021) was carried out in the Delaware Basin, an area characterized by normal faulting. As discussed by Pudugramam et al. (2021), one of the key observations from field data included optical fiber recordings in a vertical well (shown on the right side of Fig. 17b) which showed hydraulic fracture height growth of about 2600 ft (Fig. 17b). The stress profile shown in Figure 19a, uses color to represent relative values of S_{hmin} based on available well logs and DFIT tests to create a vertical profile of the magnitude of the least principal stress based on a VSR model following the methodology of Singh and Zoback (2022) as described above. Figure 17c (after Zoback et al., 2022) shows fracture aperture in color as in Fig. 16. The severe upward propagation of the hydraulic fractures is intuitively predictable from the lower stress magnitudes shown above the depth of the wells. Note that the fiber data indicates that downward propagation of the hydraulic fracture is terminated at the high stress Wolfcamp B and upward propagation ended at a lithofacies with slightly higher S_{hmin}. The hydraulic fracture colored green indicates areas where fracture propagation occurred but without proppant. Propped hydraulic fracture half lengths for the two wells are quite different at the two depths (which influences optimal well spacing) and there is modest downward growth of hydraulic fractures associated with stage position b. Elastic loading models predict higher S_{hmin} above the frac stages and limited vertical hydraulic fracture growth. The differences between the hydraulic fracture propagation of these two stages are the result of the stress magnitude differences as was seen in the case of HFTS-1. As was the case illustrated in Fig. 16, detailed modeling of lithologically-induced stress variations with depth can be used to optimize hydraulic fracturing procedures that will limit vertical transport of proppant.

5.1 Horizontal fracture propagation

While it has been known since Hubbert and Rubey (1959) that horizontal hydraulic fracture propagation is expected in reverse faulting areas when the least principal stress is the vertical stress, S_V. However, near complete stress relaxation in clay rich lithofacies (as shown in Figs. 2, 3 and 7) that results in a stress state in which the three principal stresses are approximately equal could also lead to horizontal hydraulic fractures. If hydraulic fracture propagation is not controlled by the stress field, it easiest for hydraulic fractures to propagate along sub-horizontal bedding planes with low tensile strength. While there is no direct evidence to indicate that this also occurred in the three cases shown, the implication of these case studies is that horizontal hydraulic fracture propagation may be more common than widely appreciated, regardless of whether the stress state in relatively stiff rocks is normal, normal/strike slip or strike-slip stress state. A model of both horizontal and vertical propagation in a horizontal well previously shown in Fig. 4a is shown in Fig. 18b. As would be expected, vertical hydraulic fractures are predicted near the heal of the well when the well was in a relatively brittle lithofacies and S_{hmin} is only slightly below S_V (a strike-slip/reverse faulting environment as shown in Fig. 5d) but horizontal fractures are expected when the well is in the lower, more clay rich and ductile lithofacies where $S_3 \approx S_V$ (from Dontsov et al., 2025). Thus, VSR causes S_{hmin} to increase to the magnitude of S_V and S_{Hmax} to decrease.

6 Conclusions

(1) When combined with limits on stress magnitudes from the frictional strength of faults in the crust, the concept of VSR provides reasonable values to predict lithology-dependent stress variations associated with clay + TOC rich formations typical of those being stimulated in unconventional oil and gas reservoirs.
(2) In simple terms, in normal, normal/strike-slip and strike-slip faulting areas, the VSR method predicts relatively low S_{hmin} values for stiffer rocks and relatively high S_{hmin} values for rocks with high clay + TOC and low stiffness. Elastic loading models predict the opposite relationship between S_{hmin} and stiffness. Elastic loading models which predict stress magnitudes to correlate with Young's modulus do a very poor job of matching stress measurements away from calibration points. Fundamentally, elastic loading models lead to incorrect stress profiles due to fundamentally wrong geological assumptions
(3) In some formations, complete stress relaxation can lead to the S_{hmin} being close to Sv. This has the potential to cause horizontal hydraulic fracture growth and has been observed in high clay layers in a variety of stress states.
(4) Incorrect stress profiles lead to inaccurate estimates of optimal landing zones and well spacings, and other frac-design parameters to accurately predict hydraulic fracture growth and optimize production from unconventional oil and gas reservoirs.

Acknowledgements We appreciate the contributions of collaborators at Stanford University and ResFrac. We would also like to thank the Stanford Natural Gas Initiative for financial support.

Author contribution This paper was jointly written by Mark Zoback and Ankush Singh.

Data availability Much of the data presented in this paper has either been previously published, or is freely available upon request.

Declarations

Conflict of interest The authors declare no conflict of interests.

Appendix

Two other previously-published examples illustrating the difference stress predictions using elastic loading models are presented in this Appendix. Figure 19 shows a comparison of the quantitative VSR stress prediction shown in Fig. 13 with an elastic loading model (from Singh and Zoback 2022) . Note the difference in the prediction of S_{hmin} in the Cline formation, in both cases the Cline stress measurement was not used in calibrating the model. The VSR model captures stress variations in both the Upper Wolfcamp and the Cline better than the elastic loading model. The Cline shale is generally known to be a clay and organic rich mudstone layer with relatively lower stiffness. Note that in Fig. 19, the stress profile is generated using E_{vert} in place of E_{horz}. This is done as the vertical Young's modulus is more easily available from commonly available data collected from vertical pilot wells. As the ration between the horizontal and vertical Young's modulus is unique to a given geological layer, it gets incorporated in the $n^*_{\epsilon t}$ term in Eq. 12.

McCormack et al. (2021) computed a VSR stress profile for the DJ basin in Colorado utilizing a Vertical Transverse Isotropy (VTI) seismic velocity model (Thomsen 1986) to obtain values for horizontal Young's modulus and the empirical correlation between Young's modulus and n of Ma and Zoback (2020).

Figure 20 represents pore pressure (small blue stars as determined from DFIT tests) andthe gray line shows the overburden stress, S_V, as determined from density logs. The red dashed line indicates the value of S_{hmin} for frictional equilibrium of normal faults

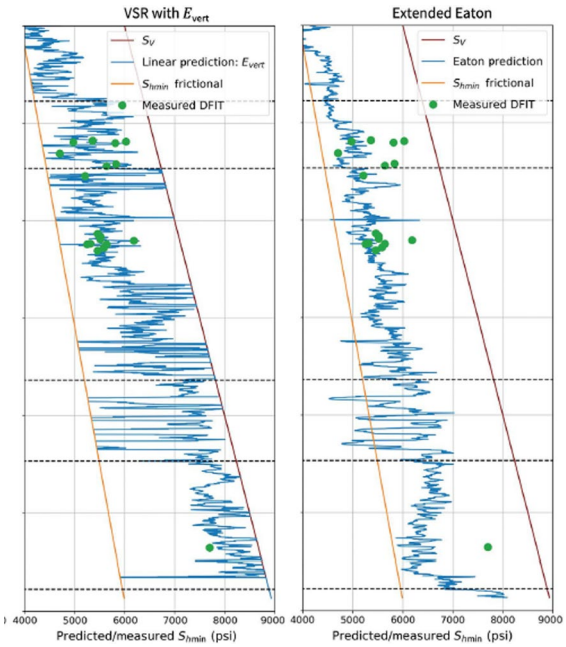

Fig. 19 Comparison of the predicted stress profiles with the measured values using the VSR methodology with the primary methodology established by Singh and Zoback 2022 (left panel), a calibrated model using the vertical Young's modulus instead of horizontal (center panel) and using the extended Eaton model (panel)

(Eq. 1). Note that measured stress values in the low clay, relatively stiff Codell sandstone are in agreement with the expected value for frictional equilibrium in this normal faulting area. The black line in Fig. 20 shows the predicted stress profile with the VSR method using the three DFIT tests in the Niobrara A and C (indicated by the red squares). The green line shows the prediction of elastic loading models using Eq. 5. Figure 20a utilizes the stress value from a DFIT test near the bottom of the Codell sandstone for calibration (indicated by c). Figure 20b utilizes the stress values from the three DFIT measurements in the Niobrara A and C (indicated by c's) to calibrate the elastic loading model. Note how markedly different the two predictions of the elastic loading model are depending on which calibration points were used. Note in Fig. 20a that S_{hmin} increases in the relatively low stiffness Niobrara A and C (as predicted by VSR) whereas the elastic loading model predicts very low S_{hmin} values in the Niobrara A and C. Figure 20b shows that the VSR method accurately predicts the stress state in the Codell sandstone much better than the elastic loading model. In the context of the vertical distribution of microearthquakes, McCormack et al. discuss why the stress model predicted using

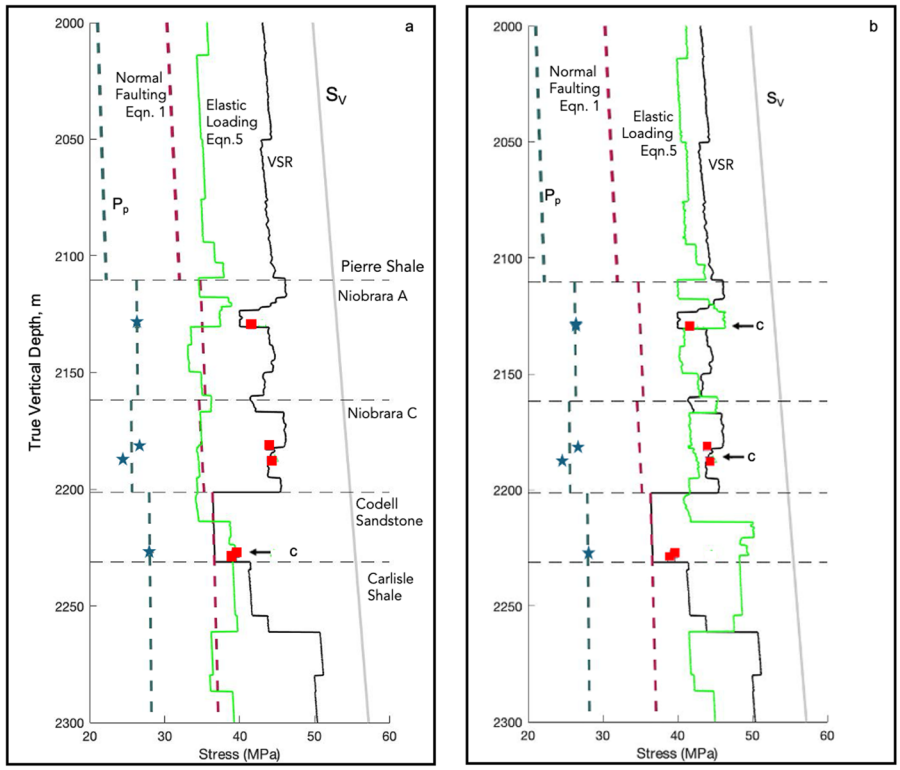

Fig. 20 Comparison of the viscoplastic stress relaxation method (black line) and elastic loading model (green line). The red squares indicate the depths of DFIT measurements available to calibrate the models. **a** The DFIT in the Codell sandstone was used to calibrate the elastic loading model. **b** The three DFITs in the Niobrara A and C were used to calibrate the elastic loading model. Modified from McCormack et al. (2021)

the VSR method better explains the vertical growth of hydraulic fractures from the unconventional wells in the Niobrara A and C.

References

Alalli AA, Zoback MD (2018) Microseismic evidence for horizontal hydraulic fractures in the Marcellus Shale, southeastern West Virginia. Lead Edge. https://doi.org/10.1190/tle37050356.1

Anderson EM (1951) The dynamics of faulting and dyke formation with applications to Britain. Oliver and Boyd, Edinburgh

Barhaug, J., Bussey, J., Schaeffer, B., Shemeta, J., Lawrence, M., Tran, J., and Stark, P., (2022) Testing XLE For Cost Savings in the DJ Basin: A Fiber Optic Case Study. In: SPE Hydraulic Fracturing Technology Conference and Exhibition, SPE, The Woodlands, Texas, USA, p D011S002R003 https://doi.org/10.2118/209155-MS

Blanton TL, Olson JE (1999) Stress magnitudes from logs: effects of tectonic strains and temperature. SPE Reserv Eval Eng 2(1):62–68

Byerlee J (1978) Friction of rocks. Pure Appl Geophys 116(4–5):615–626. https://doi.org/10.1007/BF00876528

Cipolla, C., Wolters, J., McKimmy, M., Miranda, C., Hari-Roy, S., Kechemir, A., & Gupta, N., (2022) Observation Lateral Project: Direct Measurement of Far-Field Drainage. In: SPE Hydraulic Fracturing Technology Conference and Exhibition, SPE, The Woodlands, Texas, USA, p D021S005R001 https://doi.org/10.2118/209164-MS

Dohmen T, Zhang J, Barker L, Blangy JP (2017) Microseismic magnitudes and b-values for delineating hydraulic fracturing and depletion. SPE Journal 22(5):1–11. https://doi.org/10.2118/186096-PA

Dontsov, E., Zoback, M. D., and McClure, M. W. (2026) Hydraulic fracture propagation along bedding planes might be more prevalent than we think. SPE International Hydraulic Fracturing Technology Conference and Exhibition, SPE, 226637

Eaton BA (1969) Fracture gradient prediction and its application in oilfield operations. J Pet Technol 21(10):1353–1360. https://doi.org/10.2118/2163-PA

Fowler GJ, McClure MW, Singh A, Irvin R, Ratcliff D, Ponners C, Rondon J (2024) Case studies in integrated fracture design and well spacing optimization in shale. Paper presented at the international petroleum technology conference, Dhahran, Saudi Arabia. https://doi.org/10.2523/IPTC-24396-MS

Gale JFW, Elliott SJ, Laubach SE (2018) Hydraulic fractures in core from stimulated reservoirs: core fracture description of hfts slant core, Midland Basin, West Texas. https://doi.org/10.15530/urtec-2018-2902624

Gunzburger Y, Cornet FH (2007) Rheological characterization of a sedimentary formation from a stress profile inversion. Geophys J Int 168(1):402–418. https://doi.org/10.1111/j.1365-246X.2006.03140.x

Jaeger JC, Cook NGW, Zimmerman R (2007) *Fundamentals of Rock Mechanics* (4th edition). Blackwell Publishing, Australia

Kohli A, Zoback M (2021) Stratigraphically controlled stress variations at the Hydraulic Fracture Test Site-1 in the Midland Basin, TX. Energies 14(24):8328. https://doi.org/10.3390/en14248328

Lund Snee JE, Zoback MD (2018) State of stress in the Permian Basin, Texas and New Mexico: implications for induced seismicity. Lead Edge 37(2):127–134. https://doi.org/10.1190/tle37020127.1

Lund Snee J-E, Zoback MD (2022) State of stress in areas of active unconventional oil and gas development in North America. AAPG Bull 106(2):355–385. https://doi.org/10.1306/08102120151

Ma X, Zoback MD (2017) Lithology-controlled stress variations and pad-scale faults: a case study of hydraulic fracturing in the Woodford Shale, Oklahoma. Geophysics. https://doi.org/10.1190/GEO2017-0044.1

Ma X, Zoback MD (2020) Predicting lithology-controlled stress variations in the Woodford shale from well log data via viscoplastic relaxation. SPE J. https://doi.org/10.2118/201232-pa

McClure M, Fowler G, Picone M (2022) Best practices in DFIT interpretation: comparative analysis of 62 DFITs from nine different shale plays. SPE Int Hydraul Fract Technol Conf Exhib. https://doi.org/10.2118/205297-MS

McClure M, Albrecht M, Bernet C, Cipolla C, Etcheverry K, Fowler G; Fuhr A, Gherabati A, Johnston M, Kaufman P, MacKay M, McKimmy M, Miranda C, Molina C, Ponners C, Ratcliff D, Rondon J, Singh A, Sinha R, Sung A, Xu J, Yeo J, Zinselmeyer R (2023) Results from a collaborative industry study on parent/child interactions: bakken, permian basin, and montney. Paper presented at the spe hydraulic fracturing technology conference and exhibition, The Woodlands, Texas, USA. https://doi.org/10.2118/212321-MS

McCormack KL, Zoback MD, Kuang W (2021) A case study of vertical hydraulic fracture growth, stress variations with depth and shear stimulation in the Niobrara Shale and Codell Sand, Denver-Julesburg Basin Colorado. Interpretation 9(4):SG59–SG69

McCormack KL, McLennan JD, Jagniecki EA, McPherson BJ (2023) Discrete measurements of the least horizontal principal stress from core data: an application of viscoelastic stress relaxation. SPE Reserv Eval Eng 26(03):827–841. https://doi.org/10.2118/214669-PA

Murphy, E., Rivera Barraza, S., Gu, M., Gokaraju, D., Far, M. E., Quirein, J., and Ou, L., (2015) New Models for Acoustic Anisotropic Interpretation in Shale. In: SPWLA 56th Annual Logging Symposium, OnePetro, Long Beach, California, USA

Pudugramam, V. S., Zhao, Y., Bessa, F., Li, J., Zakhour, N., Brown, T., et al., (2021) Analysis and Integration of the Hydraulic Fracturing Test Site-2 (HFTS-2) Comprehensive Dataset. In: Proceedings of the 9th Unconventional Resources Technology Conference, American Association of Petroleum Geologists, Houston, Texas, USA. https://doi.org/10.15530/urtec-2021-5241

Raterman KT, Farrell HE, Mora OS, Janssen AL, Gomez GA, Busetti S, Warren M (2017) Sampling a stimulated rock

volume: an eagle ford example, pp 24–26. https://doi.org/10.15530/urtec-20172670034
Rassouli FS, Zoback MD (2018) Comparison of short-term and long-term creep experiments in shales and carbonates from unconventional gas reservoirs. Rock Mech Rock Eng 51(7):1995–2014. https://doi.org/10.1007/s00603-018-1444-y
Sibson RH (1974) Frictional constraints on thrust, wrench and normal faults. Nature 249:542–544
Simpson RW (1997) Quantifying Anderson's fault types. J Geophys Res 102:909–919
Singh A, Shaochuan X, Mark Z, McClure M (2019) Integrated analysis of the coupling between geomechanics and operational parameters to optimize hydraulic fracture propagation and proppant distribution. Paper presented at the spe hydraulic fracturing technology conference and exhibition, The Woodlands, Texas, USA. https://doi.org/10.2118/194323-MS
Singh A, Zoback MD (2022) Predicting variations of the least principal stress with depth: application to unconventional oil and gas reservoirs using a log-based viscoelastic stress relaxation model. Geophysics. https://doi.org/10.1190/geo2021-0429.1
Sone H, Zoback MD (2013) Mechanical properties of shale-gas reservoir rocks—Part 2: ductile creep, brittle strength, and their relation to the elastic modulus. Geophysics 78(5):D393–D402
Sone H, Zoback MD (2014a) Viscous relaxation model for predicting least principal stress magnitudes in sedimentary rocks. J Pet Sci Eng. https://doi.org/10.1016/j.petrol.2014.09.022
Sone H, Zoback MD (2014b) Time-dependent deformation of shale gas reservoir rocks and its long-term effect on the in situ state of stress. Int J Rock Mech Min Sci 69:120–132. https://doi.org/10.1016/j.ijrmms.2014.04.002
Thiercelin MJ, Plumb RA (1994) Core-based prediction of lithologic stress contrasts in East Texas formations. SPE Form Eval. https://doi.org/10.2118/21847-pa
Thomsen L (1986) Weak elastic anisotropy. Geophysics 51(10):1954–1966. https://doi.org/10.1190/1.1442051
Ugueto, G. A., Haffener, J., Mondal, S., Satviski, A. A., Huckabee, P. T., and Haustveit, K., (2022) Spatial and Temporal Effects on Low Frequency DAS and Microseismic Implications on Hydraulic Fracture Geometry and Well Interactions. In: SPE Hydraulic Fracturing Technology Conference and Exhibition, SPE, The Woodlands, Texas, USA, p D021S006R001 https://doi.org/10.2118/209180-MS
Vernik L, Liu X (1997) Velocity anisotropy in shales: a petrophysical study. Geophysics 62(2):521–532
Walsh, J., Sinha, B., Donald, A., and others. (2006) Formation anisotropy parameters using borehole sonic data. In: SPWLA 47th Annual Logging Symposium
Warpinski NR, Branagan P, Wilmer R (1985) In-situ stress measurements at U. S. DOE's multiwell experiment site, Mesaverde Group, Rifle, Colorado. J Pet Technol. https://doi.org/10.2118/12142-pa
Yan D, Zhao L, Wang Y, Zhang Y, Cai Z, Song X et al (2023) Heterogeneity indexes of unconventional reservoir shales: quantitatively characterizing mechanical properties and failure behaviors. Int J Rock Mech Min Sci 171:105577. https://doi.org/10.1016/j.ijrmms.2023.105577
Zoback MD (2007) Reservoir Geomechanics. Cambridge University Press, Reservoir Geomechanics. https://doi.org/10.1017/CBO9780511586477
Zoback MD, Healy JH (1984) Friction, faulting and in situ stress. Ann Geophys 2(6):689–698
Zoback MD, Kohli AH (2019) Unconventional Reservoir Geomechanics. Cambridge University Press, United Kingdom
Zoback ML, Zoback M (1980) State of stress in the conterminous United States. J Geophys Res Solid Earth 85(B11):6113–6156. https://doi.org/10.1029/JB085iB11p06113
Zoback ML, Zoback MD, Adams J, Assumpção M, Bell S, Bergman EA et al (1989) Global patterns of tectonic stress. Nature. https://doi.org/10.1038/341291a0
Zhao Y, Bessa F, Sahni V, Liu S (2021) Key learnings from hydraulic fracturing site 2 (HFTS-2), Paper presented at unconventional resources technology conference, pp 1610–1620. https://doi.org/10.15530/urtec-2021-5229